AD 85739

23 January 1956

REPORT NO. 6R3P

COPY NO. 78

FC

ORDNANCE MISSILE LABORATORIES

Normal Force, Pitching Moment, and Center of Pressure of Eighty Cone-Cylinder-Frustum Bodies of Revolution at Mach Number 2.18 (U)

By Robert E. Lavender, James H. Henderson, and Raymond A. Deep

ORDNANCE CORPS · DEPARTMENT OF THE ARMY
REDSTONE ARSENAL
HUNTSVILLE, ALABAMA

23 January 1956

Report 6R3P

NORMAL FORCE, PITCHING MOMENT, AND CENTER OF PRESSURE OF EIGHTY CONE-CYLINDER-FRUSTUM BODIES OF REVOLUTION AT MACH NUMBER 2.18 (U)

By

Robert E. Lavender
James H. Henderson
Raymond A. Deep

ORDNANCE MISSILE LABORATORIES
Technical Feasibility Studies Office

LIBRARY ABSTRACT

A series of force tests were conducted in the Jet Propulsion Laboratory 12-inch wind tunnel at Mach numbers from 1.5 to 4.04 and angles of attack to 10 deg. This report presents normal force and pitching moment results obtained at a Mach number of 2.18 for 80 cone-cylinder-frustum configurations of systemmatically varying geometry. Initial normal force curve slope and center-of-pressure values are compared with first- and second-order potential theories.

ACKNOWLEDGMENT

The authors acknowledge the contribution of Task Corporation, Pasadena, California, to the test program through their efficient design and precise fabrication of the models and the internal strain-gage balances. We are indebted also to the personnel of the Jet Propulsion Laboratory for their cooperation throughout the planning and execution of the test program.

CONTENTS

LIST OF ILLUSTRATIONS

LIST OF ILLUSTRATIONS (Continued)

TERMS AND SYMBOLS

A_0, A_1, A_3	Coefficients in least squares equation for experimental normal force coefficient versus angle of attack
B_0, B_1, B_3	Coefficients in least squares equation for experimental pitching moment coefficient versus angle of attack
C_N	Normal force coefficient, N/qS
C_M	Pitching moment coefficient, M/qSD_{cy}
$C_{N_{10}}$	Normal force coefficient at 10-degree angle of attack
$C_{M_{10}}$	Pitching moment coefficient at 10-degree angle of attack
C'_N, A_1	Initial normal force curve slope, experimental results
C'_{N_1}	Initial normal force curve slope, first-order theory with approximate boundary conditions
$C'_{N_{1e}}$	Initial normal force curve slope, first-order theory with exact boundary conditions
C'_{N_2}	Initial normal force curve slope, hybrid theory with approximate boundary conditions
C'_M, B_1	Initial pitching moment curve slope, experimental results
D_{cy}	Cylinder diameter
L_c	Cone length
L_{cy}	Cylinder length
L_f	Frustum length
M	Pitching moment about nose, positive for nose-up moments

TERMS AND SYMBOLS (Continued)

M	Mach number
N	Normal force
N	$(\gamma + 1)M^2/2\beta^2$, in Eq. 9
q	Dynamic pressure
Q	$1 + \frac{1}{2}(\gamma - 1)M^2[1 - (1 + \phi_{0x})^2 - \phi_{0r}^2]$
R	Body radius
R'	Slope of body contour
R_{cy}	Cylinder radius
S	Reference area, πR_{cy}^2
X_{cp_0}	Initial center of pressure, experimental results, cylinder calibers aft of nose
X_{cp_1}	Initial center of pressure, first-order theory with approximate boundary conditions
$X_{cp_{1e}}$	Initial center of pressure, first-order theory with exact boundary conditions
X_{cp_2}	Initial center of pressure, hybrid theory with approximate boundary conditions
$X_{cp_{10}}$	Center of pressure at 10-degree angle of attack, experimental results
θ_c	Nose-cone half-angle, degrees
θ_f	Frustum half-angle, degrees
α	Angle of attack, degrees
β	$(M^2 - 1)^{\frac{1}{2}}$

TERMS AND SYMBOLS (Continued)

γ	Ratio of specific heats, 1.4
φ_0, φ_{0r}, φ_{0x}	First-order axial-flow perturbation potential and derivatives
ϕ_0, ϕ_{0r}, ϕ_{0x}	Second-order axial-flow perturbation potential and derivatives
φ_1, φ_{1r}, φ_{1x}	First-order cross-flow perturbation potential and derivatives

NORMAL FORCE, PITCHING MOMENT, AND CENTER OF PRESSURE OF EIGHTY CONE-CYLINDER-FRUSTUM BODIES OF REVOLUTION AT MACH NUMBER 2.18

SUMMARY

An experimental program was conducted to investigate the influence of geometric variations on the basic aerodynamic characteristics of cone-cylinder-frustum configurations. The tests were made in the Jet Propulsion Laboratory 12-inch wind tunnel at Mach numbers of 1.5, 2.18, 2.81, and 4.04 with angle-of-attack variations from −4 to 10 deg. The 80 body configurations that were tested represented variations in cone half angle of 15, 22.5, and 30 deg, variations in cylinder length of 1, 2, and 4 cylinder diameters, variations in frustum angle of 5, 10, 15, and 20 deg, and variations in frustum length from 1.2 to 6 cylinder diameters. Normal force and pitching moment data were obtained for all 80 configurations at each Mach number.

This report is the first of a series concerning this investigation and presents the basic data and analysis of the results at Mach number 2.18. The basic normal force and pitching moment data are represented by cubic equations in angle of attack with the constant coefficients determined by the least-squares procedure. Initial normal force curve slope and center of pressure as determined from the equations are presented graphically as functions of the various geometric parameters. In addition, some indication is given of the nonlinear trends of the data with angle of attack. Comparisons of the initial normal force curve slope and center of pressure are made with the first- and second-order potential theories.

INTRODUCTION

Preliminary design studies by this office of possible future Army surface-to-surface ballistic missile systems show that a separating top section design consisting of a cone, cylinder, and expanding conical frustum is a promising configuration. For any specified range and payload, many considerations must be taken into account in the top section design. Some of these considerations are

1. Effect of body shape on the drag characteristics and the corresponding effect on the dive-phase trajectory, aerodynamic heating, structural weight, and center of gravity

2. Effect of body shape on the center of pressure and stability characteristics

The cone-cylinder-frustum design is a very flexible arrangement and is capable not only of providing stability without the use of stabilizing fins but also of providing high-pressure drag, which may reduce the dive-phase velocity to an acceptable level from the standpoint of aerodynamic heating. The geometric variables of cone angle, cylinder length, frustum angle, and frustum length thus provide flexibility in selecting the proper combination for a top section design with the desired drag characteristics, stability characteristics, required volume for internal components, and, possibly, the desired base diameter.

Since very little experimental investigation has been done in the past on this type of configuration, a rather extensive experimental program was carried out using the Jet Propulsion Laboratory 12-inch supersonic wind tunnel. The primary purpose of the investigation was to obtain the initial normal force curve slope and center of pressure for a series of cone-cylinder-frustum configurations so that the results would be useful for design studies. A total of 80 configurations was chosen for testing at Mach numbers of 1.50, 2.18, 2.81, and 4.04. Angle of attack was varied up to 10 deg in order to provide some understanding of the nonlinear nature of the normal force and pitching moment characteristics. In addition, the zero-lift drag was obtained for some of the models.

The configurations consist of a nose cone of 22.5-degree half angle combined with cylinder lengths of 1, 2, and 4 cylinder calibers and frustum half angles of 5, 10, 15, and 20 deg. For each frustum angle, four variations of frustum length are considered. This results in a series of 48 configurations, all of which have, the basic 22.5-degree half-angle nose cone. Cones of 15- and 30-degree half angles are combined with the 1- and 4-caliber cylinder lengths and the 5- and 20-degree frustums, resulting in 32 additional configurations.

This report is the first of a series concerning the investigation. It presents the results of the normal force and pitching moment data for the 80 cone-cylinder-frustum configurations at a Mach number of 2.18.

MODEL AND BALANCE DESIGN

An overall view of the model configurations is shown in Fig. 1. It is convenient to define the geometric parameters by four digits, such as model 1342. The first digit defines the nose-cone half angle. The other digits define the cylinder length, frustum half angle, and frustum length, respectively. The model geometric code is presented in Table 1.

The model lengths vary from 3.066 to 11.866 cylinder calibers. In order to obtain good utilization of the 12- by 12-inch test section, two sets of model components were necessary. One set of components was designed with a cylinder diameter of 0.70 in. for the longer models, and the other set had a basic cylinder diameter of 1.20 in. for the shorter models. All models having 1- and 2-caliber cylinder lengths in combination with the first two frustum lengths (24 models) were made up of components with a basic cylinder diameter of 1.2 in. The length for the small-diameter models then varied from 3.826 to 8.306 in., whereas the length variation for the larger models varied from 3.679 to 7.448 in. These extreme models are shown in Figs. 2 and 3.

Task Corporation, Pasadena, California, was contracted for the detailed design and fabrication of the models as well as a number of strain-gage balances sufficient to cover the range of normal forces expected. The design study resulted in a relatively small number of cones, cylinders, and frustums, which assemble over a basic body sleeve for each scale. Any model could be assembled on the basic body sleeve with three components and, in some cases, a cylindrical spacer between the aft part of the sleeve and the frustum, as shown in Fig. 4. Model components were made from 4140 steel alloy with dimensions held to ±0.001 in. and with all cylindrical sections matched to ±0.0002 in. in diameter and concentricity.

Four cantilever-type internal strain-gage balances of two ranges each were required, resulting effectively in eight balances each with two moment beams. The two ranges were achieved by constructing on the same balance two sets of mutually perpendicular moment beams with different sensitivity. Either range could be selected by a simple 90-degree rotation of the balance. The balances were designed so that, for each model at each Mach number, the normal force expected would be of sufficient magnitude compared to the full-scale design load of the balance used that accurate measurements would result. In addition, the moment

beams were located to bracket the center of pressure. A photograph of all model components and balances is presented as Fig. 5.

EXPERIMENTAL PROCEDURE

The tests were performed in the Jet Propulsion Laboratory 12-inch supersonic wind tunnel.[1] The Mach number is set by means of jacks, which control the curvature of the flexible-plate nozzle. Normal operation is restricted to those Mach numbers for which flow surveys have been made. The Mach number range varies from about 1.27 to 4.04.

The internal strain-gage balances were designed to fit the Jet Propulsion Laboratory Mark VI suspension system. This system rotates in pitch about an axis passing through the center line of the test-section windows. Angle of attack is changed by means of a motor-driven worm gear, which rotates the inner portion of the suspension system. Accuracy of angle-of-attack setting is ±0.01 deg.

During the Mach number 2.18 tests, the supply pressure was maintained at 134 ± 0.5 cm Hg. The supply temperature was in the range from 80 to 95°F, and the dew point varied from 10 to -25°F.

The angle-of-attack variation was 0, -4, -2, -1, 1, 2, 4, 6, 8, 10, and 0 deg. The readings from both moment beams were plotted as the data points were obtained. Any points that appeared in error were repeated. Angle of attack was corrected for sting deflection. The normal force and pitching moment about the nose were reduced to coefficient form using the cross-sectional area of the cylinder and cylinder diameter as the reference area and length.

Reynolds number per inch at Mach number 2.18 corresponding to the supply pressure maintained for the tests was approximately a half million. Therefore, laminar flow would probably have existed over a rather large portion of some of the models except for the fact that surface roughness was applied to the nose-cone tips using number 120 grit. This roughness was applied in an effort to reduce the region of flow separation caused by shock-wave boundary-layer interaction, which was expected near the cylinder-frustum juncture. It was believed that, if the boundary layer were tripped, the resulting turbulent flow would withstand larger adverse pressure gradients, thus reducing the

region of flow separation. In addition, the boundary-layer trip effectively increases the Reynolds number and more closely similates a full-scale condition. Choice of number 120 grit was based upon previous experience of Jet Propulsion Laboratory personnel concerning boundary-layer trips.[2] Photographs of two models and a nose cone with grit are shown in Fig. 6.

During the course of the tests, normal force and pitching moment data were obtained for a few models with and without nose grit. Although some small differences in the data occurred, no definite conclusions could be drawn from the small number of comparative tests. Comparisons of the flow field about typical models with and without nose grit are shown in the Schlieren photographs of Figs. 7 to 9. All the experimental results discussed in the following sections apply for models with the nose grit.

EXPERIMENTAL RESULTS

In a search for a satisfactory method of presenting the results, it was found that cubic equations of the form

$$C_N = A_0 + A_1\alpha + A_3\alpha^3 \qquad (1)$$

and

$$C_M = B_0 + B_1\alpha + B_3\alpha^3 \qquad (2)$$

represented excellently the experimental results. The coefficients of these equations were obtained by the least-squares procedure. An indication of the accuracy of equations 1 and 2 in reproducing the experimental data can be obtained from Figs. 10 to 13. In these figures the experimental points for typical models are shown as the circles, and the least-square fairing, as the solid line. The least-squares curves deviate only a small amount from the data points.

Before the least-squares curve was computed for each run, careful attention was given to obtain the best set of data points. Any data points that were not in line were investigated for errors in data reduction. Data points that were clearly in error were omitted in the least-squares procedure so that the computed curves would not be affected adversely by such points.

All the A_0 and B_0 values are very small, which means only a slight zero shift is required to align the curves through the origin. Therefore, the experimental data are considered defined by the equations.

$$C_N = A_1\alpha + A_3\alpha^3 \tag{3}$$

and

$$C_M = B_1\alpha + B_3\alpha^3 \tag{4}$$

Values of the initial normal force curve slope, A_1, are given in Table 2. The values corresponding to the basic configurations with a 22.5-degree half-angle nose cone are plotted in Figs. 14 to 16. These slopes, based on the cylinder cross-sectional area, naturally increase with increasing frustum length or frustum angle. The initial slopes based upon the base area, however, decrease with increasing frustum length or frustum angle, as can be seen from Table 3. The value 0.0349 per degree given by slender-body theory is seen to agree quite well for long, slender bodies. The effect of increasing nose-cone angle or cylinder length is seen to reduce the initial normal force curve slope slightly in most cases.

Values of initial pitching moment curve slope, B_1, are tabulated in Table 4, and the initial center of pressure in cylinder calibers aft of the nose is given in Table 5. The initial center-of-pressure values for the basic configurations with a 22.5-degree half-angle nose cone are shown in Figs. 17 to 19. The initial center of pressure in cylinder calibers aft of nose naturally increases with increasing cylinder length, frustum length, or frustum angle.

The initial center-of-pressure values in percent body length are given in Table 6, and it may be seen that the effect of increasing cylinder length is to decrease these values for configurations with short frustum lengths. An opposite effect is obtained for configurations with long frustum lengths.

Initial center of pressure in cylinder calibers aft of the cone-cylinder juncture is given in Table 7. It may be observed that the effect of increasing cone angle is to shift the initial center of pressure slightly rearward with respect to the cone-cylinder juncture. The consistency of the results in showing such small effects is a measure of the accuracy of the overall test data and analysis procedure.

Although the constants A_3 and B_3 for each run well define the nonlinear characteristics of the normal force and pitching moment data, the constants are not very consistent functions of the geometric parameters. They are so small that large percentage changes in these constants can be made in most cases with only negligible changes in the normal force and pitching moment coefficients. These constants multiplied by 1000 are listed for the various models in Tables 8 and 9. The values correspond to the increments in normal force and pitching moment coefficients resulting from nonlinearity at 10-degree angle of attack.

Even though the terms A_3 and B_3 are very small, certain trends appear as shown by Tables 8 and 9: In general, the A_3 term increases with increasing cylinder length or frustum length but decreases with increasing frustum angle. The trend seems to indicate an increasing (negative) B_3 term with increasing cylinder of frustum length and decreasing (negative) values with increasing frustum angle.

The relative importance of the nonlinear increment in normal force coefficient in relation to the contribution of the linear term is shown in Table 10. The term $[1 + (100\ A_3/A_1)]$ is shown and is a measure of the importance of the nonlinear term in the normal force coefficient at 10-degree angle of attack. This is seen by rewriting equation 3.

$$C_N = A_1\alpha \left[1 + \left(\frac{100A_3}{A_1}\right) \frac{\alpha^2}{100}\right] \tag{5}$$

The nonlinear term is relatively important for the longer cylinder lengths and smaller frustum angles, but it is rather unimportant for the shorter cylinder lengths and larger frustum angles.

Corresponding values for the term $[1 + (100\ B_3/B_1)]$ are shown in Table 11. The increment in pitching moment coefficient due to nonlinearity at 10-degree angle of attack is seen to vary from about 0 to 65% of the linear contribution.

The center of pressure is given by

$$X_{cp} = \frac{-C_M}{C_N} = \frac{-B_1\alpha - B_3\alpha^3}{A_1\alpha + A_3\alpha^3} = \frac{-B_1}{A_1}\left[\frac{1 + (B_3/B_1)\alpha^2}{1 + (A_3/A_1)\alpha^2}\right] \tag{6}$$

or at 10-degree angle of attack

$$\frac{X_{cp_{10}}}{X_{cp_0}} = \frac{1 + (100B_3/B_1)}{1 + (100A_3/A_1)} \tag{7}$$

The ratio of the center of pressure at 10-degree angle of attack to the initial value is shown in Table 12. Most of the configurations have a rearward shift in center of pressure with increasing angle of attack. This ratio tends to decrease with increasing frustum length or frustum angle so that for large frustum lengths and frustum angles this ratio becomes less than unity, thus producing a forward shift in center of pressure with increasing angle of attack. For such configurations, the initial center of pressure is more rearward than the center of pressure of the nonlinear force caused by cross flow.

The effect of increasing cone angle tends to increase the values of these nonlinear parameters, although the effect is so small that the results are not entirely consistent. These nonlinear parameters for the basic configurations with 22.5-degree half-angle nose cone are shown in Figs. 20 to 22. The fairings used for the center-of-pressure data are consistent with the fairings for the normal force and moment data.

THEORETICAL PROCEDURE

Supersonic potential-flow theories have been used to calculate the initial normal force curve slope and center of pressure for all the models except those with a 30-degree half-angle nose cone since, at Mach number 2.18, the limits of potential theory are exceeded.

First-order and second-order perturbation equations for axial flow[3, 4] have been solved using approximate boundary conditions. These equations with their corresponding boundary conditions are

(First-order Axial Flow)

$$\varphi_{0rr} + \frac{\varphi_{0r}}{R} - \beta^2 \varphi_{0xx} = 0 \tag{8}$$

$$\text{B. C.} \quad \varphi_{0r} = R'$$

and

(Second-order Axial Flow)

$$\phi_{0rr} + \frac{\phi_{0r}}{R} - \beta^2 \phi_{0xx} = M^2 \left[2(N-1)\beta^2 \varphi_{0x} \varphi_{0xx} + 2\varphi_{0r}\varphi_{0xr} + \varphi^2_{0r} \varphi_{0rr}\right] \tag{9}$$

$$\text{B. C.} \quad \phi_{0r} = R'(1 + \varphi_{0x})$$

The first-order perturbation equation for cross flow has been solved also using the approximate boundary condition

(First-order Cross Flow)

$$\varphi_{1rr} + \frac{\varphi_{1r}}{R} - \frac{\varphi_1}{R^2} - \beta^2 \varphi_{1xx} = 0 \tag{10}$$

$$\text{B. C.} \quad \varphi_{1r} = -1$$

First-order axial-flow and cross-flow perturbation velocities obtained from solutions of equations 8 and 10 have been used to obtain the first-order normal force curve slope distribution[5]

$$\frac{dC'_{N_1}}{dX} = \frac{2R\varphi_{1x}}{R^2_{cy}} \left(1 - \beta^2 \varphi_{0x}\right) \tag{11}$$

The second-order axial-flow perturbation velocities have been combined with first-order cross-flow perturbation velocities to provide a hybrid solution for the normal force slope distribution.[6]

$$\frac{dC'_{N_2}}{dX} = \frac{2R\varphi_{1x}}{R^2_{cy}} \left(1 + R'^2\right)\left(1 + \phi_{0x}\right) Q^{1/\gamma - 1} \tag{12}$$

The initial normal force curve slopes were obtained by numerically integrating the distributions over the body lengths.

A previous theoretical investigation[7] of the cone-cylinder-frustum type of body also has been used to obtain the first-order solution for the normal force curve slope and center of pressure for a limited number of the models where the exact boundary conditions were used in the solution of equations 8 and 10. Certain cross plots of these data were necessary to obtain the values corresponding to the models at Mach number 2.18. Only data for configurations with 22.5-degree half-angle nose cone and base-to-cylinder diameter ratios of 3 or less could be obtained.

It has been general practice to consider the pitching moment curve slope distribution for slender bodies to be given by

$$\frac{dC'_M}{dX} = \left(\frac{dC'_N}{dX}\right) X \tag{13}$$

However, for blunt bodies a consideration of the axial-force effect on the pitching moment shows that the pitching moment curve slope distribution is given by[7]

$$\frac{dC'_M}{dX} = \frac{dC'_N}{dX} (X + RR') \tag{14}$$

For example, the initial center of pressure of a cone, given by the ratio of C'_M to C'_N, is not $(2/3)L_c$ but $(2/3)L_c \sec^2 \theta_c$.

All initial center-of-pressure values computed for the models were obtained by dividing the total initial pitching moment curve slope, including both normal and axial force effects, by the initial normal force curve slope.

EXPERIMENTAL AND THEORETICAL COMPARISONS

Comparison of the initial normal force curve slope with theoretical results is given in Table 13. In general, the theories predict larger values than actually occur. First-order theory using the approximate boundary conditions, C'_{N_1}, is as much as 25% too high for models with long cylinders and small frustums (model 2311). Best agreement of this theory with the experimental results occurs for model 1341 where the error is only about 4%. Better agreement is obtained for the models with the smaller cone angle. The effect of using the exact boundary conditions is to improve the agreement for all models that were compared.

Hybrid theory is better than first-order theory in almost all cases, the approximate boundary conditions being used. The results indicate, therefore, that best agreement would be obtained using hybrid theory with the exact boundary conditions. Unfortunately, no solutions have been obtained by this procedure for comparison. Use of the exact boundary conditions complicates the hybrid theory calculations, and the improvement over first-order theory with exact boundary conditions may not be worth the effort.

Comparison of the initial center of pressure with theoretical results is given in Table 14. In general, the various theoretical calculations are in good agreement with the experimental results, being within ±0.05 cylinder caliber in many cases. Such agreement appears to be within the accuracy of the test data. The difference between first-order and hybrid theory appears to be very small, using the approximate boundary conditions, whereas the difference between using the approximate or exact boundary conditions shows a larger effect. For some models, the use of approximate boundary conditions results in better agreement with experimental results, whereas the use of exact boundary conditions is better for others.

No comparisons are made between the experimental nonlinear characteristics and theory. Most cross-flow theories are based upon the cross-flow drag of a circular cylinder and predict larger nonlinear effects with increasing model planform area. Although the experimental data show larger nonlinear effects with increasing planform area obtained by increasing cylinder length or frustum length, the opposite effect is obtained with increasing planform area obtained by increasing

frustum angle. Any cross-flow theory that could be expected to correlate well with experimental data for configurations of this type would have to take these effects into account.

CONCLUSIONS

1. An expanding conical frustum attached to the rear of a cone-cylinder body is an effective means for providing static stability.

2. The initial normal force curve slope and center of pressure for cone-cylinder-frustum configurations can be obtained from the presented results over a broad range of geometric parameters.

3. The experimental normal force and pitching moment data are well defined by equations to the third degree in angle of attack, the coefficients of these equations being obtained by least squares.

4. The increment in normal force and pitching moment due to nonlinearity at angle of attack generally increases with increasing cylinder or frustum length but decreases with increasing frustum angle.

5. First-order potential flow theory using approximate boundary conditions generally predicts larger initial normal force curve slopes than occur. For the models with a 22.5-degree half-angle cone, the average error is about 20% and does not vary much with body geometry.

6. Use of exact boundary conditions with the first-order theory improves agreement with the experimental initial normal force results, and the agreement becomes better with increasing frustum angle.

7. The initial normal force curve slope by hybrid theory is better than first-order theory in almost all cases, the approximate boundary conditions being used. For the models with a 22.5-degree half-angle cone, the average error is about 15% and does not vary much with body geometry.

8. Agreement between the theoretical initial center of pressure, with the effect of axial force on the pitching moment being considered, and experimental results is very good, being within ±0.05 cylinder caliber in many cases.

9. The difference in theoretical initial center-of-pressure values between linear theories using approximate and exact boundary conditions is greater than the difference between linear and hybrid theories where approximate boundary conditions are used.

REFERENCES

1. Puckett, Allen E., Performance of the 12-inch Wind Tunnel, Jet Propulsion Laboratory Memorandum 4-52, 1 June 1949.

2. Luther, Marvin, Fixing Boundary-layer Transition on Supersonic Wind-tunnel Models, Jet Propulsion Laboratory Progress Report 20-256, 12 August 1955.

3. Van Dyke, Milton D., Practical Calculation of Second-order Supersonic Flow Past Nonlifting Bodies of Resolution, NACA TN 2744, July 1952.

4. Lavender, Robert E., Second-order and Hybrid Supersonic Flow Theories with Modifications and a Detailed Computational Procedure, Redstone Arsenal Report 6R1P, 15 February 1954.

5. Dorrance, W. H., A Supersonic Body Profile Development Study, Report 2, First Order and Linearized Theories for Supersonic Flow Around Bodies of Revolution with Experiments at Mach Number 1.90, University of Michigan Report UMM-54, 1 June 1950, Confidential.

6. Van Dyke, Milton D., First- and Second-order Theory of Supersonic Flow Past Bodies of Revolution, Journal of the Aeronautical Sciences, March 1951.

7. Deep, Raymond A., and Henderson, James H., Study of Aerodynamic Characteristics of Cone-Cylinder—Conical Frustum Bodies by Linearized Theory of Supersonic Flow, Redstone Arsenal Report 6R2P, 8 June 1955.

Table 1
Model Geometric Code

Each model is designated by four digits, such as model 1342. The first digit defines the nose-cone half-angle. The other digits define the cylinder length, frustum half-angle, and frustum length, respectively. Angles are given in degrees; lengths, in cylinder calibers.

First Digit	θ_c	Second Digit	L_{cy}	Third Digit	θ_f
1	15.0	1	1	1	5
2	22.5	2	2	2	10
3	30.0	3	4	3	15
				4	20

Fourth Digit	L_f $\theta_f = 5$	$\theta_f = 10$	$\theta_f = 15$	$\theta_f = 20$
1	1.5	1.4	1.3	1.2
2	3.0	2.8	2.6	2.4
3	4.5	4.2	3.9	3.6
4	6.0	5.6	5.2	4.8

θ_c Nose-cone half-angle, degrees
L_{cy} Cylinder length, cylinder calibers
θ_f Frustum half-angle, degrees
L_f Frustum length, cylinder calibers

Table 2
Initial Normal Force Curve Slope

$$A_1 = C'_N$$

Model	11XX	21XX	31XX	22XX	13XX	23XX	33XX
XX11	0.0649	0.0660	0.0646	0.0668	0.0573	0.0617	0.0594
XX12	0.0878	0.0889	0.0841	0.0850	0.0835	0.0816	0.0791
XX13	0.1144	0.1153	0.1094	0.1108	0.1144	0.1140	0.1100
XX14	0.1480	0.1476	0.1421	0.1482	0.1476	0.1461	0.1431
XX21		0.0792		0.0770		0.0732	
XX22		0.1280		0.1227		0.1218	
XX23		0.1914		0.1939		0.1858	
XX24		0.2814		0.2698		0.2703	
XX31		0.0915		0.0888		0.0874	
XX32		0.1686		0.1625		0.1649	
XX33		0.2747		0.2705		0.2692	
XX34		0.4195		0.4132		0.4098	
XX41	0.1041	0.1036	0.0971	0.1017	0.1072	0.1034	0.0992
XX42	0.2124	0.2090	0.2000	0.2040	0.2085	0.2001	0.1967
XX43	0.3643	0.3573	0.3506	0.3500	0.3570	0.3460	0.3452
XX44	0.5743	0.5655	0.5587	0.5579	0.5552	0.5468	0.5452

Table 3
Initial Normal Force Curve Slope
Based on Base Area

$$C'_{N_b} = C'_N \left(\frac{R_{cy}}{R_b}\right)^2$$

Model	11XX	21XX	31XX	22XX	13XX	23XX	33XX
XX11	0.0408	0.0414	0.0406	0.0419	0.0360	0.0387	0.0373
XX12	0.0378	0.0383	0.0362	0.0366	0.0360	0.0351	0.0341
XX13	0.0358	0.0361	0.0342	0.0347	0.0358	0.0357	0.0344
XX14	0.0352	0.0351	0.0338	0.0353	0.0351	0.0348	0.0341
XX21		0.0355		0.0345		0.0328	
XX22		0.0324		0.0310		0.0308	
XX23		0.0311		0.0315		0.0302	
XX24		0.0318		0.0305		0.0306	
XX31		0.0318		0.0309		0.0304	
XX32		0.0294		0.0284		0.0288	
XX33		0.0288		0.0283		0.0282	
XX34		0.0293		0.0288		0.0286	
XX41	0.0296	0.0295	0.0276	0.0290	0.0305	0.0294	0.0282
XX42	0.0281	0.0277	0.0265	0.0270	0.0276	0.0265	0.0260
XX43	0.0278	0.0273	0.0268	0.0267	0.0272	0.0264	0.0263
XX44	0.0284	0.0280	0.0277	0.0276	0.0275	0.0271	0.0270

Table 4
Initial Pitching Moment Curve Slope
(with Sign Changed)

$$-B_1 = -C'_M$$

Model	11XX	21XX	31XX	22XX	13XX	23XX	33XX
XX11	0.1480	0.1216	0.1021	0.1279	0.1594	0.1262	0.1086
XX12	0.2650	0.2185	0.1850	0.2321	0.3337	0.2754	0.2516
XX13	0.4469	0.3814	0.3323	0.4156	0.6315	0.5532	0.5112
XX14	0.7206	0.6231	0.5615	0.7198	1.0203	0.9122	0.8564
XX21		0.1582		0.1728		0.1988	
XX22		0.3754		0.4208		0.5514	
XX23		0.7625		0.9018		1.1362	
XX24		1.3936		1.5660		2.0143	
XX31		0.1974		0.2222		0.2845	
XX32		0.5386		0.6207		0.8505	
XX33		1.1680		1.3634		1.7927	
XX34		2.2109		2.5338		3.2356	
XX41	0.2999	0.2385	0.1950	0.2779	0.4768	0.3879	0.3427
XX42	0.8492	0.7017	0.6152	0.8326	1.2981	1.1067	1.0380
XX43	1.8394	1.5742	1.4451	1.8322	2.7048	2.4043	2.3003
XX44	3.4602	3.0536	2.8420	3.5153	4.8431	4.4207	4.2501

Table 5
Initial Center of Pressure

$$X_{cp_0} = -\frac{B_1}{A_1}$$

Model	11XX	21XX	31XX	22XX	13XX	23XX	33XX
XX11	2.28	1.84	1.58	1.92	2.75	2.05	1.83
XX12	3.02	2.46	2.20	2.73	4.00	3.38	3.18
XX13	3.91	3.31	3.04	3.75	5.52	4.85	4.65
XX14	4.87	4.22	3.95	4.86	6.91	6.25	5.99
XX21		2.00		2.24		2.71	
XX22		2.93		3.43		4.53	
XX23		3.98		4.65		6.12	
XX24		4.95		5.80		7.45	
XX31		2.16		2.50		3.26	
XX32		3.20		3.82		5.16	
XX33		4.25		5.04		6.66	
XX34		5.27		6.13		7.90	
XX41	2.88	2.30	2.01	2.73	4.45	3.75	3.45
XX42	4.00	3.36	3.08	4.08	6.23	5.53	5.28
XX43	5.05	4.41	4.12	5.24	7.58	6.95	6.66
XX44	6.03	5.40	5.09	6.30	8.72	8.09	7.80

Table 6
Initial Center of Pressure
in Percent Body Length

$(X_{cp_0} / L_t)\ 100$

Model	11XX	21XX	31XX	22XX	13XX	23XX	33XX
XX11	52.2	49.6	46.9	40.8	37.3	30.6	28.7
XX12	51.5	47.2	45.2	44.0	45.1	41.2	40.4
XX13	53.1	49.4	47.8	48.7	53.3	50.0	49.6
XX14	54.9	51.4	50.2	52.8	58.2	55.8	55.1
XX21		55.4		48.6		41.0	
XX22		58.5		57.1		56.6	
XX23		62.1		62.8		65.1	
XX24		63.4		65.9		68.9	
XX31		61.6		55.5		50.1	
XX32		66.6		65.8		66.1	
XX33		69.6		70.9		73.1	
XX34		71.1		72.9		75.9	
XX41	70.8	67.5	65.6	61.9	63.0	58.5	56.9
XX42	76.0	72.9	72.2	72.8	75.4	72.7	72.7
XX43	78.1	75.9	75.4	77.0	80.1	78.9	78.7
XX44	78.7	77.1	76.4	78.7	81.8	80.8	80.7

Table 7
Initial Center of Pressure Measured
aft of Cone-Cylinder Juncture

$$\bar{X}_{cp_0} = X_{cp_0} - L_c$$

Model	11XX	21XX	31XX	22XX	13XX	23XX	33XX
XX11	0.42	0.64	0.71	0.71	0.89	0.84	0.96
XX12	1.15	1.25	1.34	1.52	2.13	2.17	2.31
XX13	2.04	2.10	2.17	2.54	3.66	3.65	3.78
XX14	3.00	3.01	3.09	3.65	5.05	5.04	5.12
XX21		0.79		1.04		1.51	
XX22		1.73		2.22		3.32	
XX23		2.78		3.44		4.91	
XX24		3.75		4.60		6.25	
XX31		0.95		1.30		2.05	
XX32		1.99		2.61		3.95	
XX33		3.05		3.83		5.45	
XX34		4.06		4.93		6.69	
XX41	1.01	1.10	1.14	1.53	2.58	2.55	2.59
XX42	2.13	2.15	2.21	2.88	4.36	4.32	4.41
XX43	3.18	3.20	3.26	4.03	5.71	5.74	5.80
XX44	4.16	4.19	4.22	5.09	6.86	6.88	6.93

Table 8
Values of $A_3 \times 10^3$

Model	11XX	21XX	31XX	22XX	13XX	23XX	33XX
XX11	0.0714	0.0563	0.0384	0.0734	0.2145	0.1782	0.1683
XX12	0.1115	0.1015	0.1202	0.1390	0.1955	0.1997	0.1856
XX13	0.1749	0.1280	0.1702	0.1622	0.2600	0.2271	0.2476
XX14	0.1887	0.1860	0.1888	0.2291	0.2526	0.2468	0.2505
XX21		0.0293		0.0816		0.1624	
XX22		0.0867		0.1237		0.1593	
XX23		0.1234		0.1377		0.1636	
XX24		0.1329		0.1593		0.1707	
XX31		0.0170		0.0718		0.1276	
XX32		0.0725		0.1123		0.1397	
XX33		0.1086		0.1119		0.1164	
XX34		0.1574		0.1504		0.1217	
XX41	0.0236	0.0118	0.0150	0.0645	0.0837	0.0945	0.1106
XX42	0.0652	0.0597	0.0804	0.1045	0.0360	0.0941	0.1041
XX43	0.0531	0.0928	0.0993	0.1186	0.0445	0.1285	0.1471
XX44	0.1319	0.1730	0.1733	-0.0325	0.0116	0.0613	0.1111

Table 9
Values of $-B_3 \times 10^3$

Model	11XX	21XX	31XX	22XX	13XX	23XX	33XX
XX11	0.2300	0.1324	0.1137	0.3057	0.9368	0.7910	0.7152
XX12	0.4623	0.3888	0.3993	0.5781	0.9983	0.9347	0.8503
XX13	0.8389	0.5527	0.7384	0.7636	1.3560	1.1683	1.2161
XX14	1.0208	0.9838	0.9691	1.2369	1.4951	1.4010	1.4449
XX21		0.0998		0.2807		0.6589	
XX22		0.3287		0.5103		0.6326	
XX23		0.5254		0.5590		0.7162	
XX24		0.8482		0.8638		0.8054	
XX31		0.0682		0.2474		0.4657	
XX32		0.2730		0.4530		0.4783	
XX33		0.5361		0.5060		0.3830	
XX34		0.8719		0.8734		0.4472	
XX41	0.0875	0.0490	0.0858	0.2220	0.1284	0.2459	0.3893
XX42	0.2407	0.2344	0.3056	0.3776	-0.2366	0.2445	0.2950
XX43	0.2425	0.4839	0.4721	0.6044	-0.1314	0.4298	0.5467
XX44	0.7202	0.8407	0.9243	-0.4623	-0.5303	-0.0340	0.2468

Table 10

Values of $\frac{C_{N_{10}}}{10C'_N} = 1 + \frac{100A_3}{A_1}$

Model	11XX	21XX	31XX	22XX	13XX	23XX	33XX
XX11	1.110	1.085	1.059	1.110	1.374	1.289	1.283
XX12	1.127	1.114	1.143	1.164	1.234	1.245	1.235
XX13	1.153	1.111	1.156	1.146	1.227	1.199	1.225
XX14	1.128	1.126	1.133	1.155	1.171	1.169	1.175
XX21		1.037		1.106		1.222	
XX22		1.068		1.101		1.131	
XX23		1.065		1.071		1.088	
XX24		1.047		1.059		1.063	
XX31		1.019		1.081		1.146	
XX32		1.043		1.069		1.085	
XX33		1.040		1.041		1.043	
XX34		1.038		1.036		1.030	
XX41	1.023	1.011	1.015	1.063	1.078	1.091	1.111
XX42	1.031	1.029	1.040	1.051	1.017	1.047	1.053
XX43	1.015	1.026	1.028	1.034	1.012	1.037	1.043
XX44	1.024	1.031	1.031	0.994	1.002	1.011	1.020

Table 11

Values of $\frac{C_{M_{10}}}{10C'_M} = 1 + \frac{100B_3}{B_1}$

Model	11XX	21XX	31XX	22XX	13XX	23XX	33XX
XX11	1.155	1.109	1.111	1.239	1.588	1.627	1.659
XX12	1.174	1.178	1.216	1.249	1.299	1.339	1.338
XX13	1.188	1.145	1.222	1.184	1.215	1.211	1.238
XX14	1.142	1.158	1.173	1.172	1.147	1.154	1.169
XX21		1.063		1.162		1.332	
XX22		1.088		1.121		1.115	
XX23		1.069		1.062		1.063	
XX24		1.061		1.055		1.040	
XX31		1.035		1.111		1.164	
XX32		1.051		1.073		1.056	
XX33		1.046		1.037		1.021	
XX34		1.039		1.034		1.014	
XX41	1.029	1.021	1.044	1.080	1.027	1.063	1.114
XX42	1.028	1.033	1.050	1.045	0.982	1.022	1.029
XX43	1.013	1.031	1.033	1.033	0.995	1.018	1.024
XX44	1.021	1.028	1.033	0.987	0.989	0.999	1.006

Table 12

Values of $\frac{X_{cp_{10}}}{X_{cp_0}} = \frac{1 + (100B_3/B_1)}{1 + (100A_3/A_1)}$

Model	11XX	21XX	31XX	22XX	13XX	23XX	33XX
XX11	1.041	1.022	1.049	1.116	1.134	1.262	1.293
XX12	1.042	1.057	1.064	1.073	1.053	1.076	1.083
XX13	1.030	1.031	1.057	1.033	0.990	1.010	1.011
XX14	1.012	1.028	1.035	1.015	0.980	0.987	0.995
XX21		1.025		1.051		1.090	
XX22		1.019		1.018		0.986	
XX23		1.004		0.992		0.977	
XX24		1.013		0.996		0.978	
XX31		1.016		1.028		1.016	
XX32		1.008		1.004		0.973	
XX33		1.006		0.996		0.979	
XX34		1.001		0.998		0.984	
XX41	1.006	1.010	1.029	1.016	0.953	0.974	1.003
XX42	0.997	1.004	1.010	0.994	0.966	0.976	0.977
XX43	0.998	1.005	1.005	0.999	0.983	0.982	0.982
XX44	0.997	0.997	1.002	0.993	0.987	0.988	0.986

Table 13
Comparison of Initial Normal Force Curve Slope
with Theoretical Results

Model	C'_N	C'_{N_1}	Error, %	C'_{N_2}	Error, %	$C'_{N_{1e}}$	Error, %
2111	0.0660	0.0809	22.6	0.0756	14.5	0.0760	15.2
2112	0.0889	0.1067	19.9	0.1005	12.9	0.1015	14.0
2113	0.1153	0.1365	18.4	0.1296	12.4	0.1314	14.0
2114	0.1476	0.1711	15.9	0.1637	10.9	0.1670	13.1
2121	0.0792	0.0943	19.1	0.0852	7.6	0.0882	11.4
2122	0.1280	0.1523	19.0	0.1412	10.3	0.1414	10.5
2123	0.1914	0.2283	19.3	0.2150	12.3	0.2130	11.3
2124	0.2814	0.3219	14.4	0.3062	8.8	0.2990	6.3
2131	0.0915	0.1077	17.7	0.1025	12.0	0.0980	7.1
2132	0.1686	0.2006	19.0	0.1928	14.4	0.1796	6.5
2133	0.2747	0.3299	20.1	0.3187	16.0		
2134	0.4195	0.4944	17.9	0.4790	14.2		
2141	0.1036	0.1247	20.4	0.1207	16.5	0.1080	4.2
2142	0.2090	0.2533	21.2	0.2479	18.6	0.2100	0.5
2143	0.3573	0.4386	22.8	0.4308	20.6		
2144	0.5655	0.6792	20.1	0.6681	18.1		

Table 13 (Continued)

Model	C'_N	C'_{N_1}	Error, %	C'_{N_2}	Error, %	$C'_{N_{1e}}$	Error, %
2211	0.0668	0.0809	21.1	0.0757	13.3	0.0750	12.3
2212	0.0850	0.1041	22.5	0.0983	15.6	0.0990	16.5
2213	0.1108	0.1338	20.8	0.1275	15.1	0.1281	15.6
2214	0.1482	0.1691	14.1	0.1622	9.4	0.1640	10.7
2221	0.0770	0.0949	23.2	0.0886	15.1	0.0860	11.7
2222	0.1227	0.1489	21.4	0.1411	15.0	0.1378	12.3
2223	0.1939	0.2237	15.4	0.2140	10.4	0.2076	7.1
2224	0.2698	0.3172	17.6	0.3052	13.1	0.2928	8.9
2231	0.0888	0.1081	21.7	0.1028	15.8	0.0957	7.8
2232	0.1625	0.1960	20.6	0.1887	16.1	0.1682	3.5
2233	0.2705	0.3229	19.4	0.3127	15.6		
2234	0.4132	0.4863	17.7	0.4721	14.3		
2241	0.1017	0.1204	18.4	0.1160	14.1	0.1040	2.3
2242	0.2040	0.2427	19.0	0.2375	16.4	0.2030	-0.5
2243	0.3500	0.4244	21.3	0.4173	19.2		
2244	0.5579	0.6628	18.8	0.6527	17.0		

Table 13 (Continued)

Model	C'_N	C'_{N_1}	Error, %	C'_{N_2}	Error, %	$C'_{N_{1e}}$	Error, %
2311	0.0617	0.0771	25.0	0.0721	16.9	0.0722	17.0
2312	0.0816	0.1009	23.7	0.0956	17.2	0.0960	17.6
2313	0.1140	0.1323	16.1	0.1265	11.0	0.1260	10.5
2314	0.1461	0.1689	15.6	0.1627	11.4	0.1633	11.8
2321	0.0732	0.0836	14.2	0.0785	7.2	0.0836	14.2
2322	0.1218	0.1377	13.1	0.1314	7.9	0.1332	9.4
2323	0.1858	0.2139	15.1	0.2060	10.9	0.2035	9.5
2324	0.2703	0.3088	14.2	0.2990	10.6	0.2910	7.7
2331	0.0874	0.1009	15.4	0.0960	9.8	0.0921	5.4
2332	0.1649	0.1880	14.0	0.1817	10.2	0.1680	1.9
2333	0.2692	0.3159	17.3	0.3069	14.0		
2334	0.4098	0.4808	17.3	0.4682	14.3		
2341	0.1034	0.1143	10.5	0.1145	10.7	0.0992	- 4.1
2342	0.2001	0.2353	17.6	0.2352	17.5	0.1980	- 1.0
2343	0.3460	0.4174	20.6	0.4158	20.2		
2344	0.5468	0.6570	20.2	0.6527	19.4		

Table 13 (Continued)

Model	C'_N	C'_{N_1}	Error, %	C'_{N_2}	Error, %
1111	0.0649	0.0716	10.3	0.0691	6.5
1112	0.0878	0.0958	9.1	0.0929	5.8
1113	0.1143	0.1252	9.5	0.1220	6.7
1114	0.1480	0.1599	8.0	0.1563	5.6
1311	0.0573	0.0665	16.1	0.0640	11.7
1312	0.0835	0.0904	8.3	0.0877	5.0
1313	0.1144	0.1220	6.6	0.1191	4.1
1314	0.1476	0.1591	7.8	0.1560	5.7
1141	0.1041	0.1122	7.8	0.1108	6.4
1142	0.2124	0.2374	11.8	0.2354	10.8
1143	0.3643	0.4203	15.4	0.4169	14.4
1144	0.5743	0.6593	14.8	0.6532	13.7
1341	0.1072	0.1032	- 3.7	0.1017	- 5.1
1342	0.2085	0.2243	7.6	0.2225	6.7
1343	0.3570	0.4064	13.8	0.4029	12.9
1344	0.5552	0.6460	16.4	0.6402	15.3

Table 14
Comparison of Initial Center of Pressure
with Theoretical Results

Model	X_{cp_0}	X_{cp_1}	X_{cp_2}	$X_{cp_{1e}}$	Model	X_{cp_0}	X_{cp_1}	X_{cp_2}	$X_{cp_{1e}}$
2111	1.84	1.74	1.73	1.81	2211	1.92	1.87	1.87	1.92
2112	2.46	2.41	2.42	2.44	2212	2.73	2.69	2.73	2.75
2113	3.31	3.21	3.24	3.24	2213	3.75	3.66	3.71	3.70
2114	4.22	4.09	4.13	4.07	2214	4.86	4.68	4.75	4.68
2121	2.00	1.95	1.91	2.04	2221	2.24	2.21	2.24	2.25
2122	2.93	2.92	2.93	3.00	2222	3.43	3.41	3.45	3.49
2123	3.98	3.92	3.96	4.11	2223	4.65	4.58	4.64	4.76
2124	4.95	4.92	4.97	5.12	2224	5.80	5.70	5.75	5.84
2131	2.16	2.12	2.13	2.14	2231	2.50	2.46	2.49	2.44
2132	3.20	3.20	3.22	3.18	2232	3.82	3.81	3.85	3.79
2133	4.25	4.23	4.26		2233	5.04	5.01	5.04	
2134	5.27	5.23	5.26		2234	6.13	6.09	6.12	
2141	2.30	2.27	2.29	2.24	2241	2.73	2.65	2.70	2.56
2142	3.36	3.38	3.41	3.30	2242	4.08	4.07	4.12	3.94
2143	4.41	4.40	4.42		2243	5.24	5.24	5.27	
2144	5.40	5.37	5.39		2244	6.30	6.28	6.31	

Table 14 (Continued)

Model	X_{cp_0}	X_{cp_1}	X_{cp_2}	$X_{cp_{1e}}$	Model	X_{cp_0}	X_{cp_1}	X_{cp_2}
2311	2.05	1.99	2.00	2.11	1111	2.28	2.21	2.21
2312	3.38	3.12	3.18	3.42	1112	3.02	2.97	2.98
2313	4.85	4.53	4.61	4.76	1113	3.91	3.85	3.87
2314	6.25	5.83	5.93	6.00	1114	4.87	4.79	4.82
2321	2.71	2.31	2.33	2.69	1141	2.88	2.83	2.85
2322	4.53	4.34	4.41	4.55	1142	4.00	4.04	4.06
2323	6.12	5.98	6.05	6.13	1143	5.05	5.09	5.10
2324	7.45	7.33	7.39	7.41	1144	6.03	6.07	6.08
2331	3.26	3.00	3.06	3.03	1311	2.75	2.49	2.49
2332	5.16	5.07	5.14	5.06	1312	4.00	4.01	4.06
2333	6.66	6.60	6.66		1313	5.52	5.46	5.53
2334	7.90	7.85	7.89		1314	6.91	6.83	6.87
2341	3.75	3.38	3.58	3.27	1341	4.45	4.08	4.15
2342	5.53	5.48	5.58	5.33	1342	6.23	6.26	6.31
2343	6.95	6.93	6.97		1343	7.58	7.69	7.71
2344	8.09	8.10	8.12		1344	8.72	8.85	8.86

Model Configurations

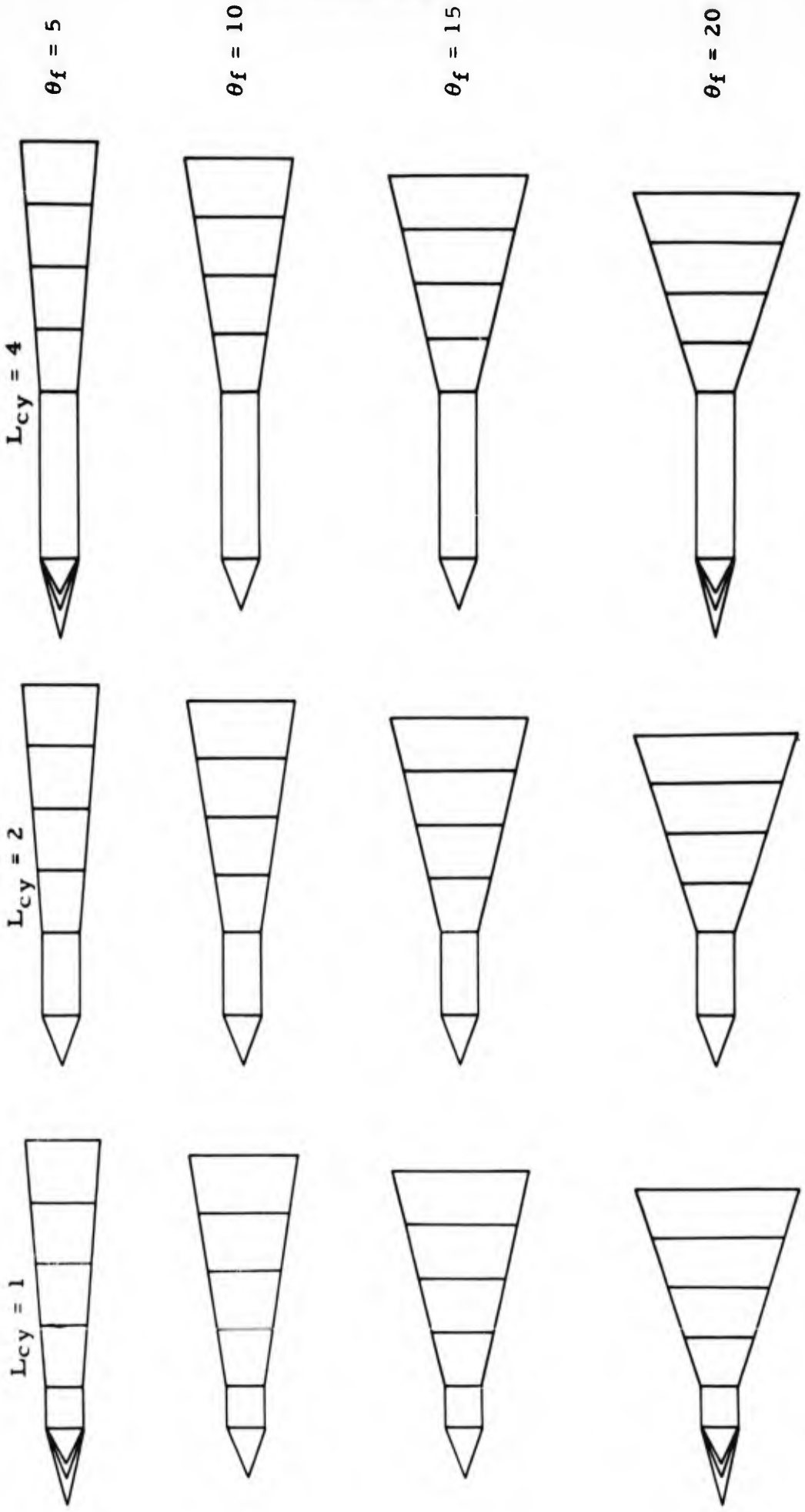

Fig. 1

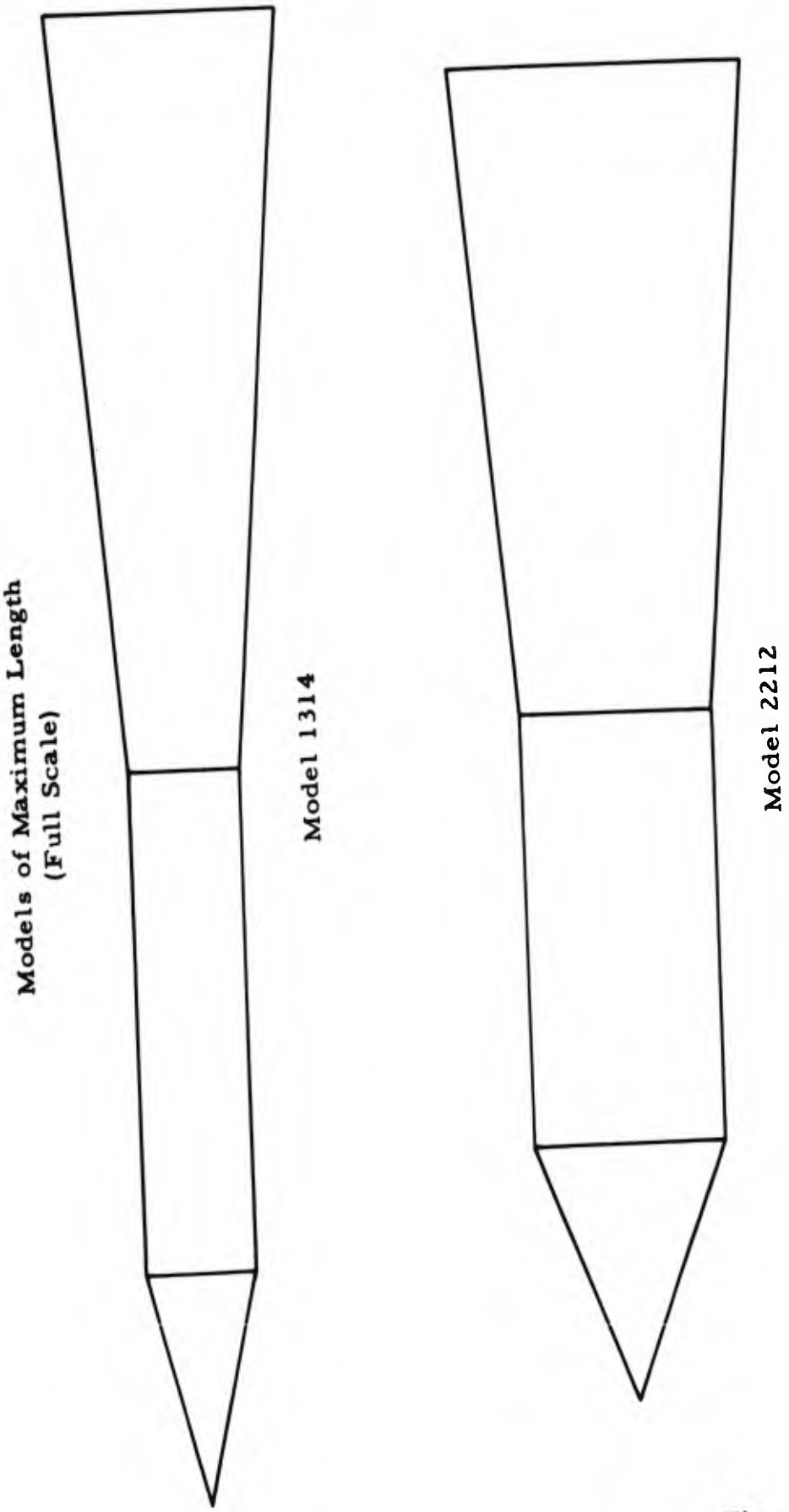

Fig. 2

Models of Minimum Length
(Full Scale)

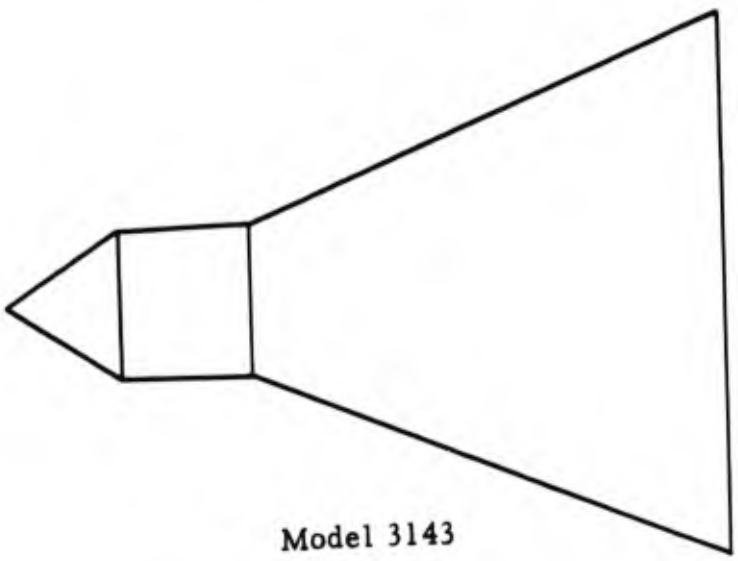

Model 3143

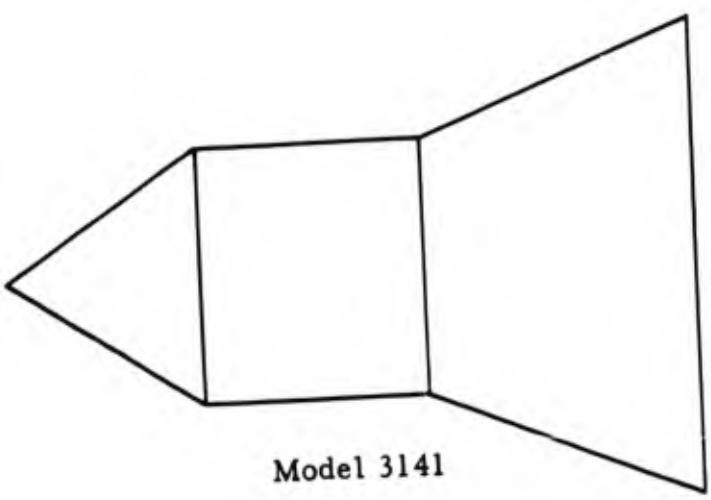

Model 3141

Fig. 3

Model Assembly

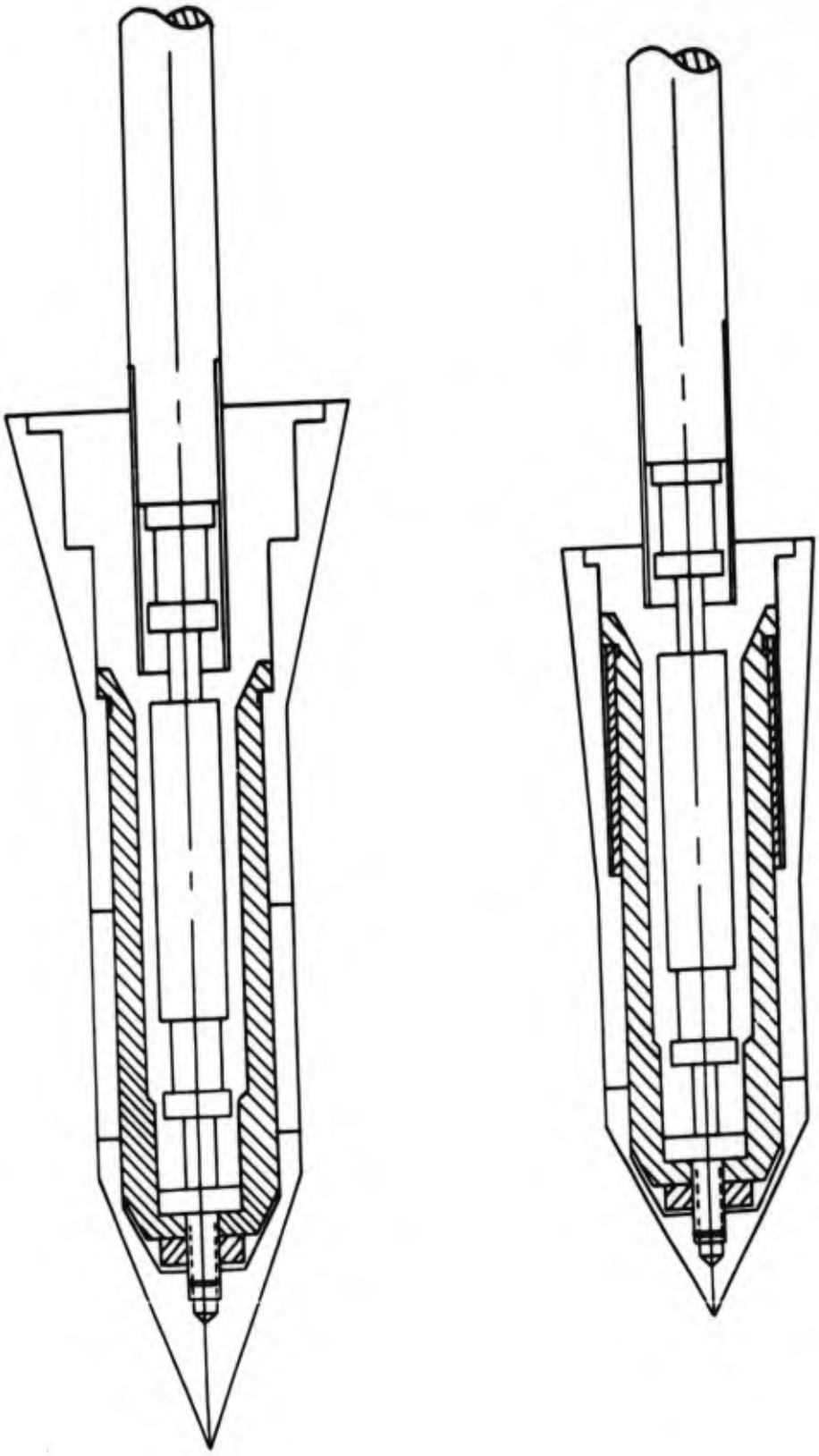

Fig. 4

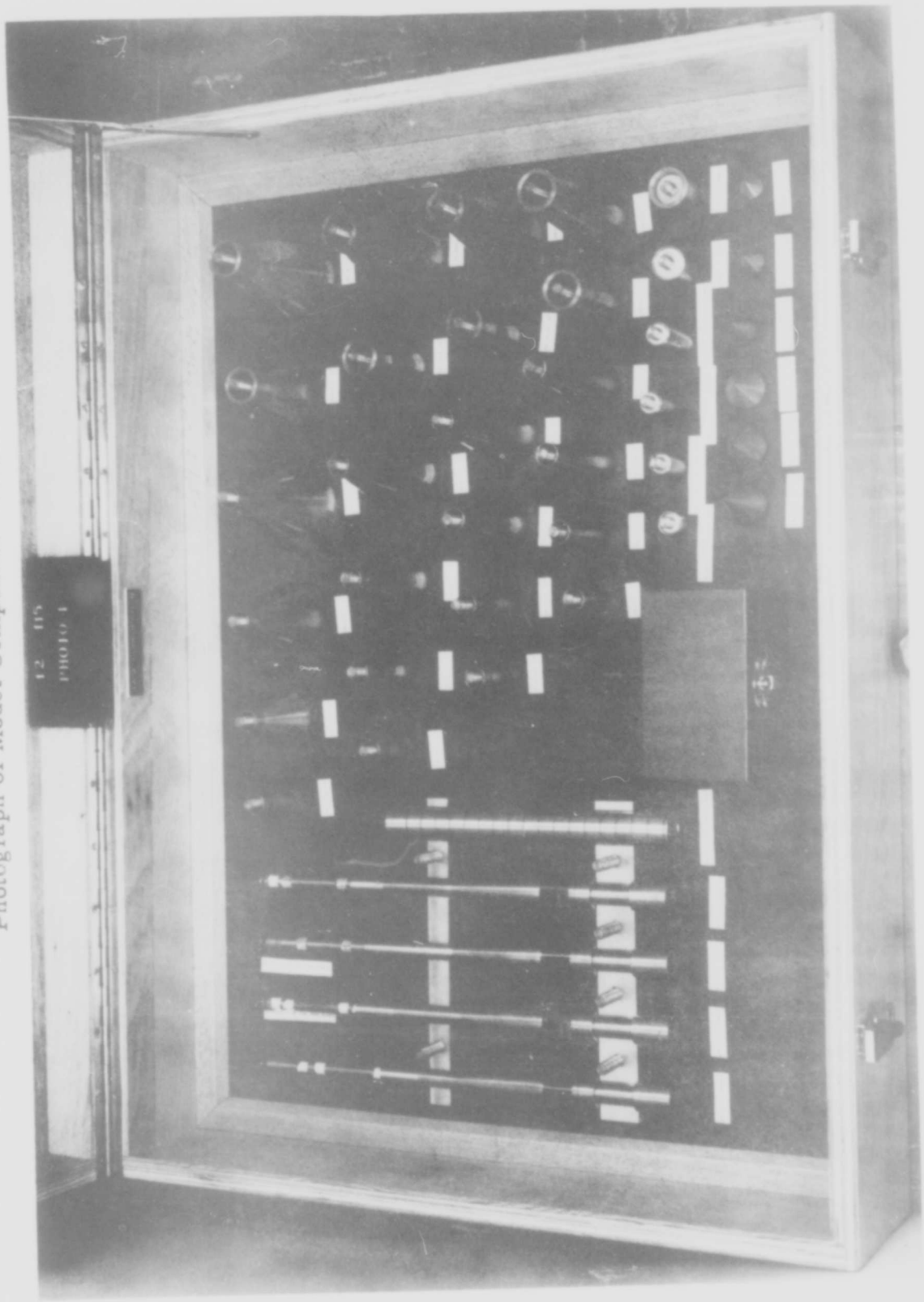

Photograph of Model Components and Balances

Fig. 5

Photographs of Models 1313 and 3142

Model 1313

No. 120 Nose Grit

Model 3142

Fig. 6

Schlieren Photographs of Model 1142
$\theta_c = 15$, $L_{cy} = 1$, $\theta_f = 20$, $L_f = 2.4$

$\alpha = 0$
No Grit

$\alpha = 0$
With Grit

$\alpha = 10$
No Grit

$\alpha = 10$
With Grit

Fig. 7

Schlieren Photographs of Model 3142
$\theta_c = 30$, $L_{cy} = 1$, $\theta_f = 20$, $L_f = 2.4$

$\alpha = 0$
No Grit

$\alpha = 0$
With Grit

$\alpha = 10$
No Grit

$\alpha = 10$
With Grit

Fig. 8

Schlieren Photographs of Models 1314 and 1344 with Nose Grit

Model 1314: $\theta_c = 15$, $L_{cy} = 4$, $\theta_f = 5$, $L_f = 6$

$\alpha = 0$

$\alpha = 10$

Model 1344: $\theta_c = 15$, $L_{cy} = 4$, $\theta_f = 20$, $L_f = 4.8$

$\alpha = 0$

$\alpha = 10$

Fig. 9

Normal Force Coefficient Vs. Angle of Attack
for Models 2311, 2312, 2313, and 2314

$\theta_c = 22.5$, $L_{cy} = 4$, $\theta_f = 5$

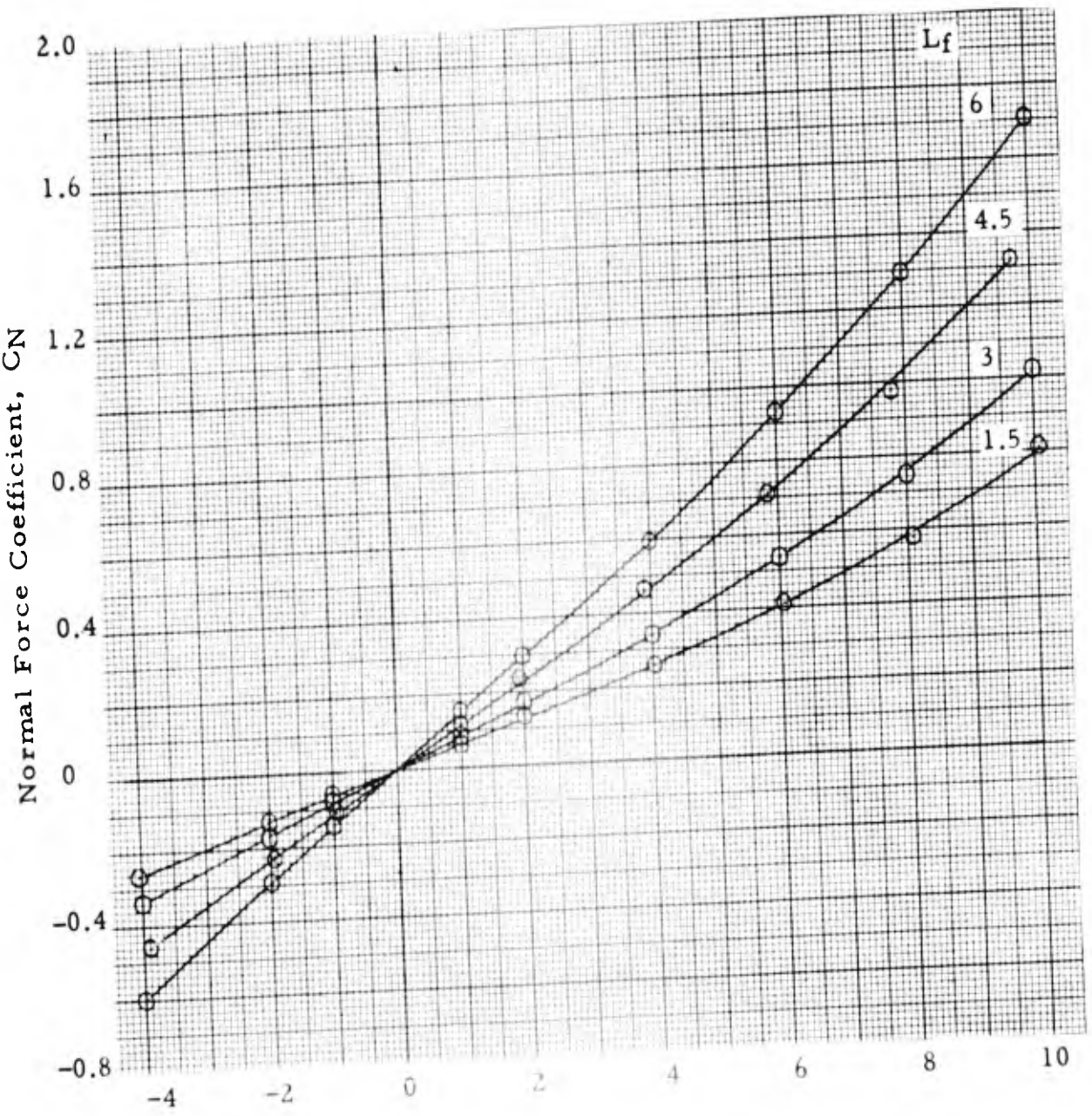

Fig. 10

Pitching Moment Coefficient Vs. Angle of Attack
for Models 2311, 2312, 2313, and 2314

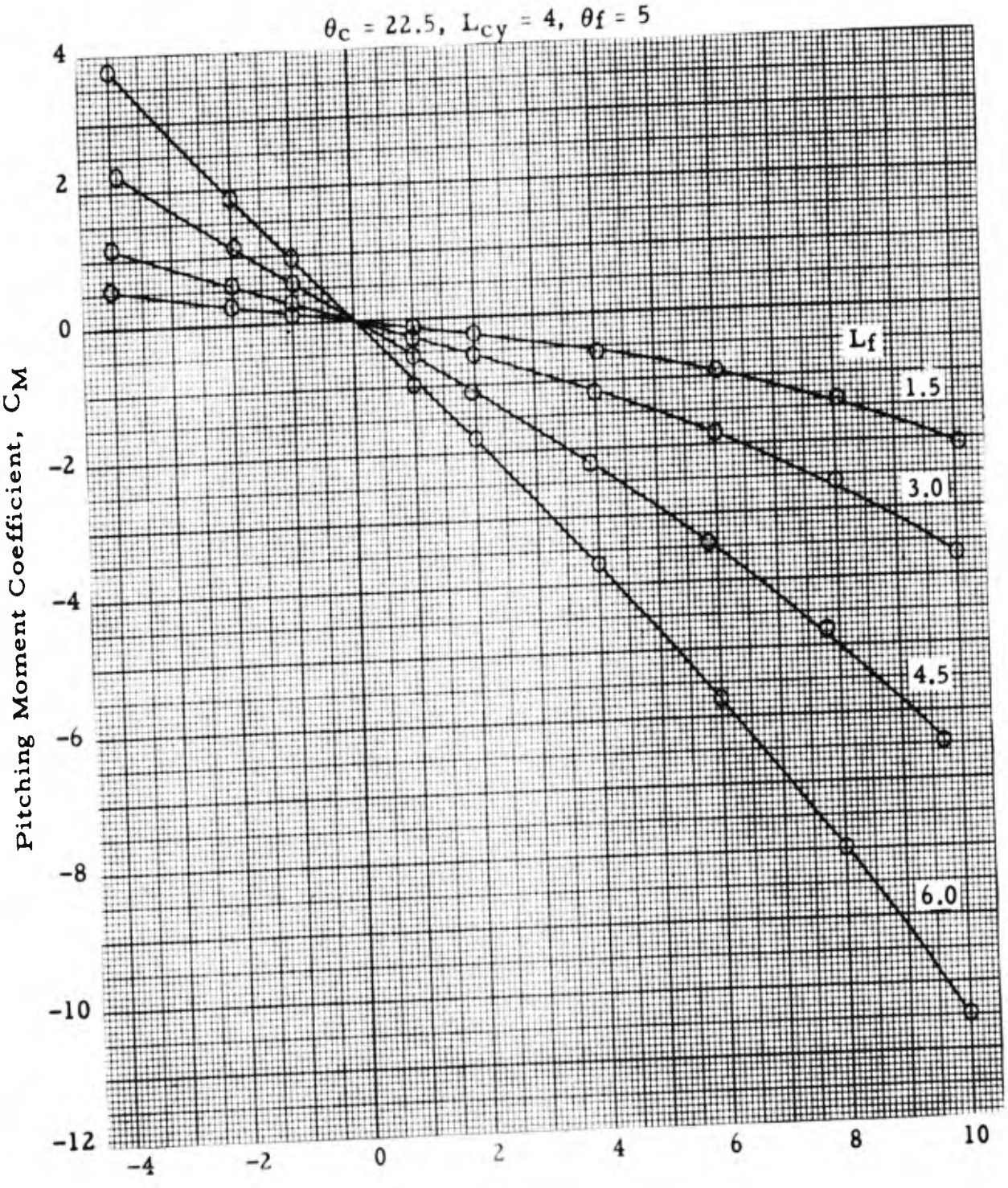

Fig. 11

Normal Force Coefficient Vs. Angle of Attack
for Models 2141, 2142, 2143, and 2144

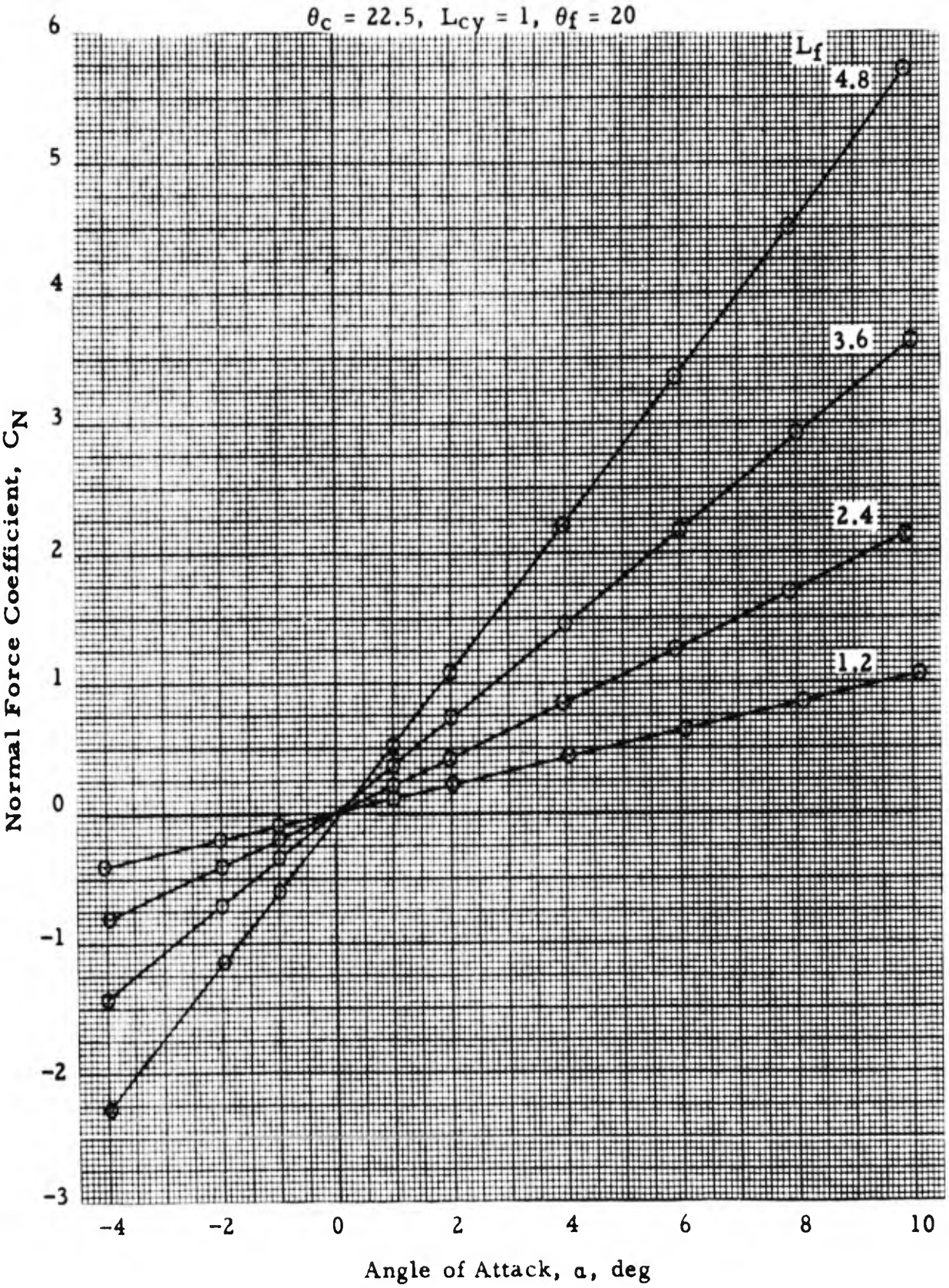

Fig. 12

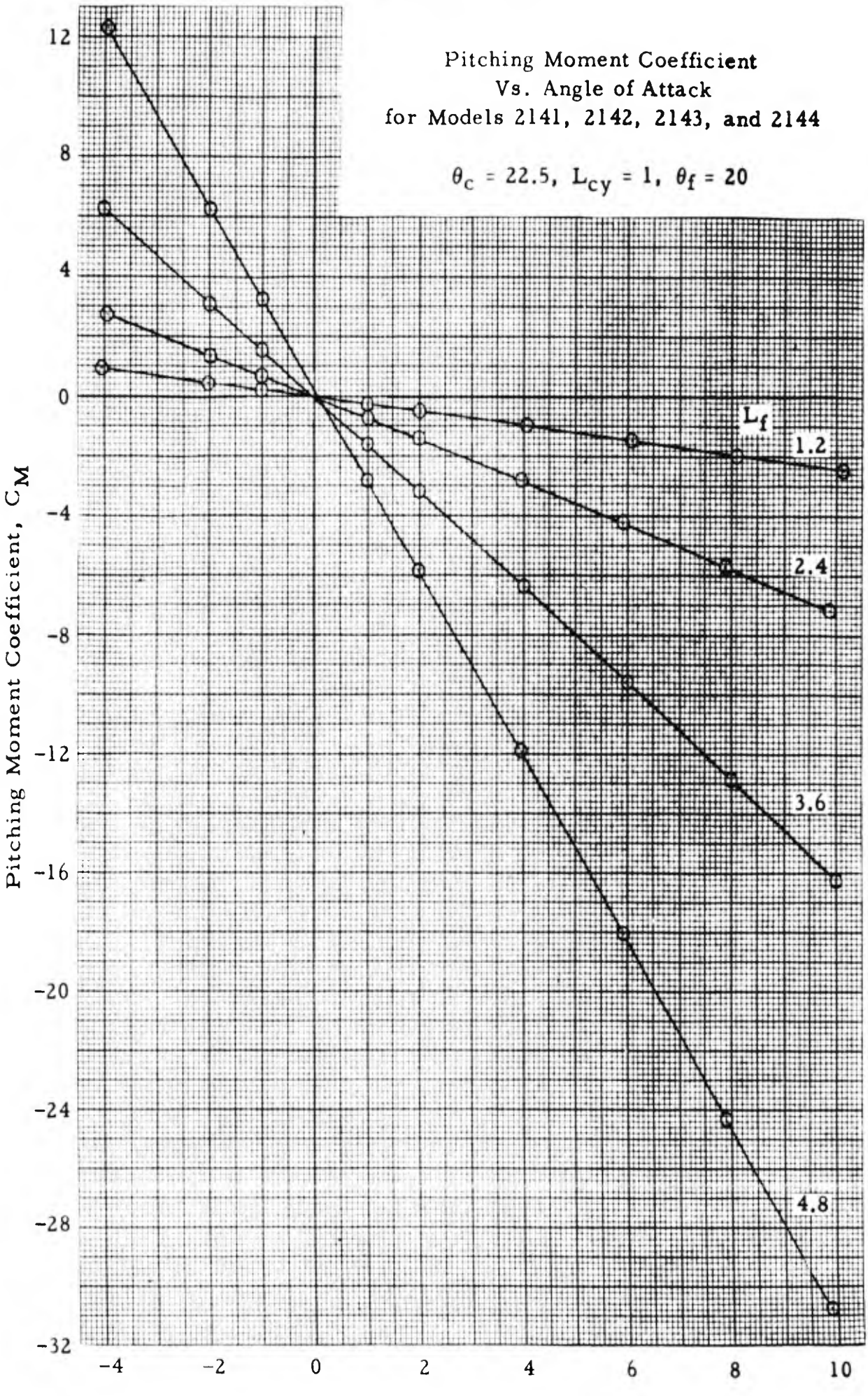
Pitching Moment Coefficient
Vs. Angle of Attack
for Models 2141, 2142, 2143, and 2144
θ_c = 22.5, L_{cy} = 1, θ_f = 20
L_f
1.2
2.4
3.6
4.8
Pitching Moment Coefficient, C_M
12
8
4
0
-4
-8
-12
-16
-20
-24
-28
-32
-4
-2
0
2
4
6
8
10
Angle of Attack, α, deg

Fig. 13

Initial Normal Force Curve Slope for Models 21XX

$\theta_c = 22.5,\ L_{cy} = 1$

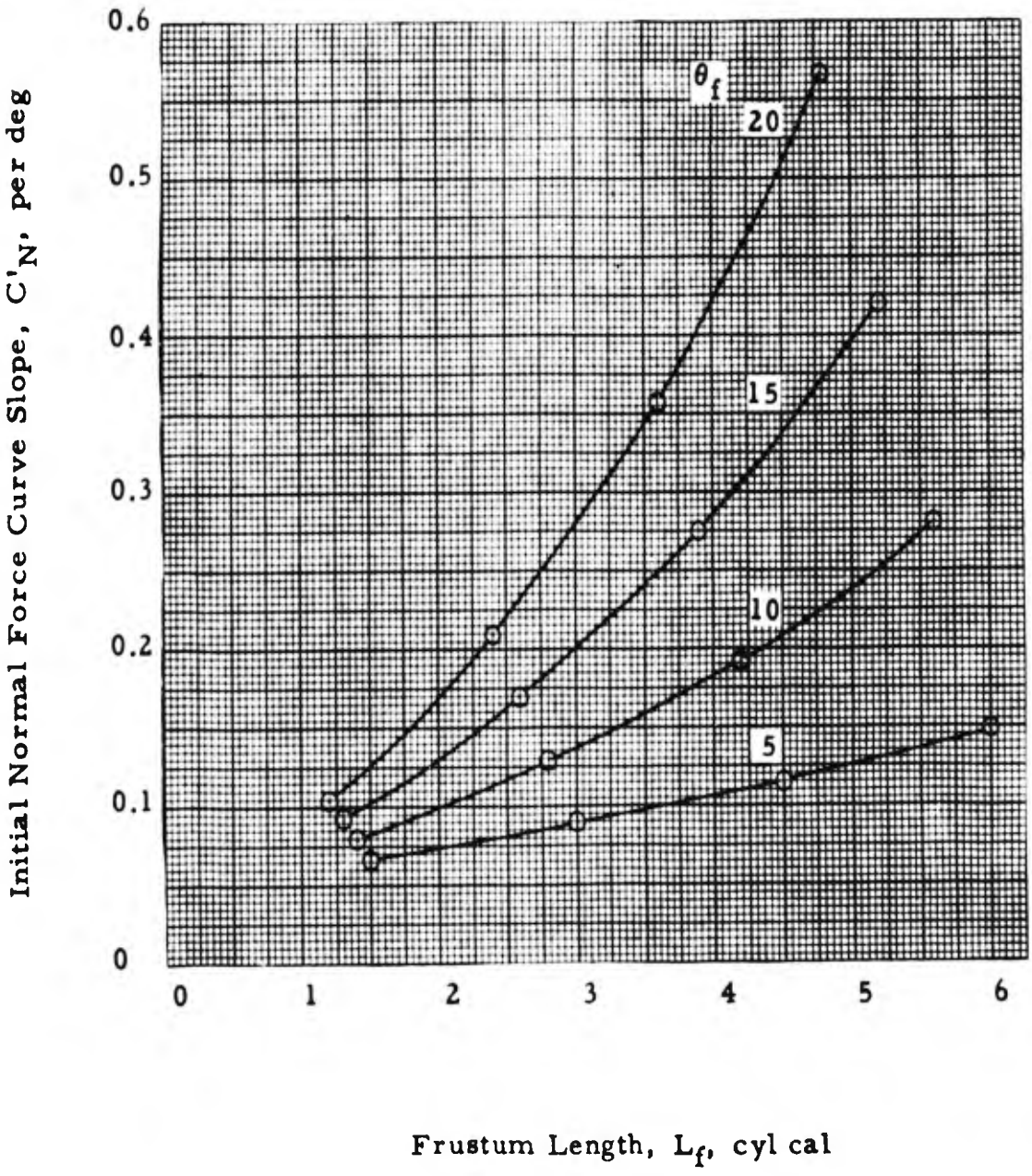

Fig. 14

Initial Normal Force Curve Slope for Models 22XX

$\theta_c = 22.5$, $L_{cy} = 2$

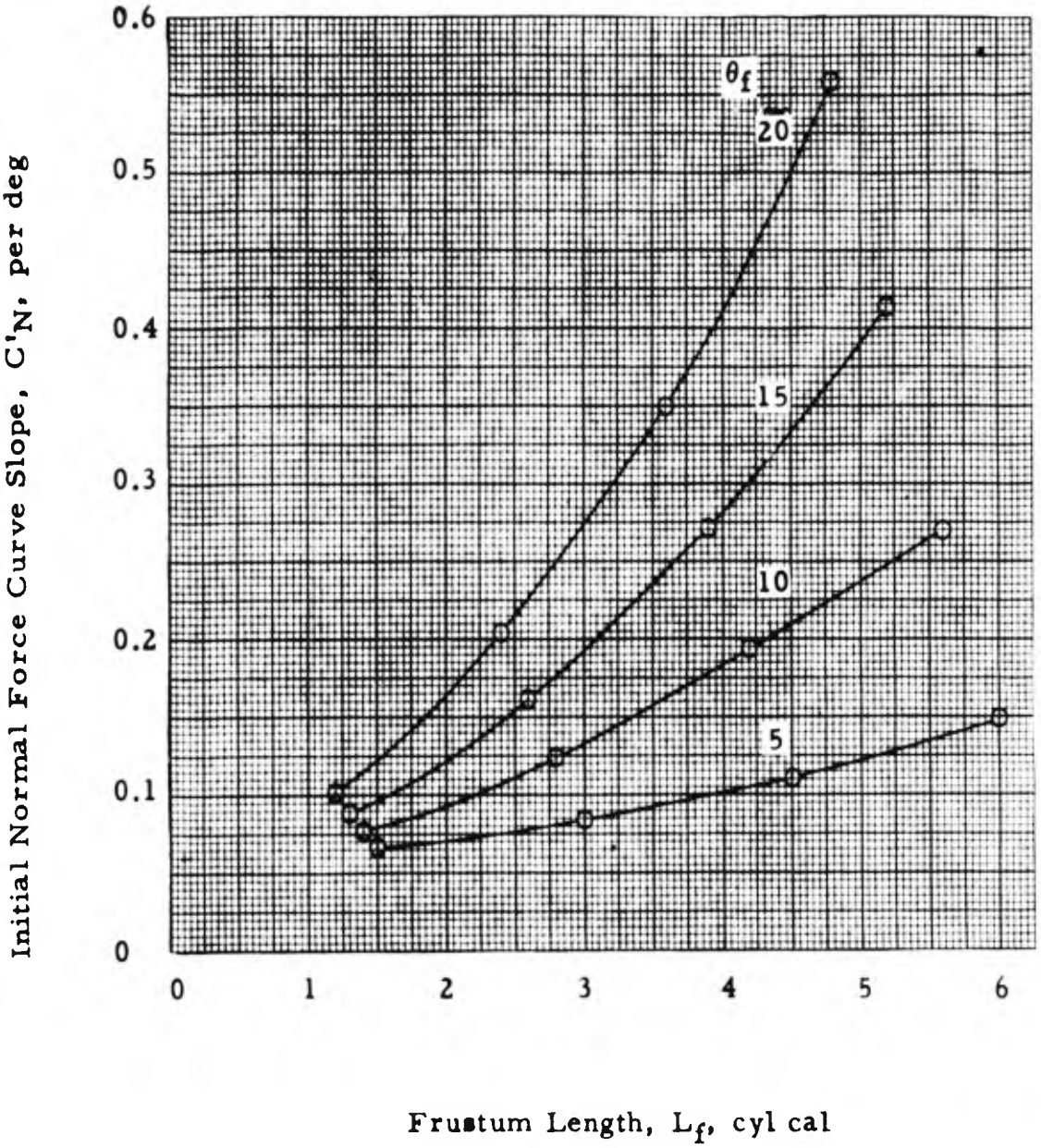

Fig. 15

Initial Normal Force Curve Slope for Models 23XX

$\theta_c = 22.5$, $L_{cy} = 4$

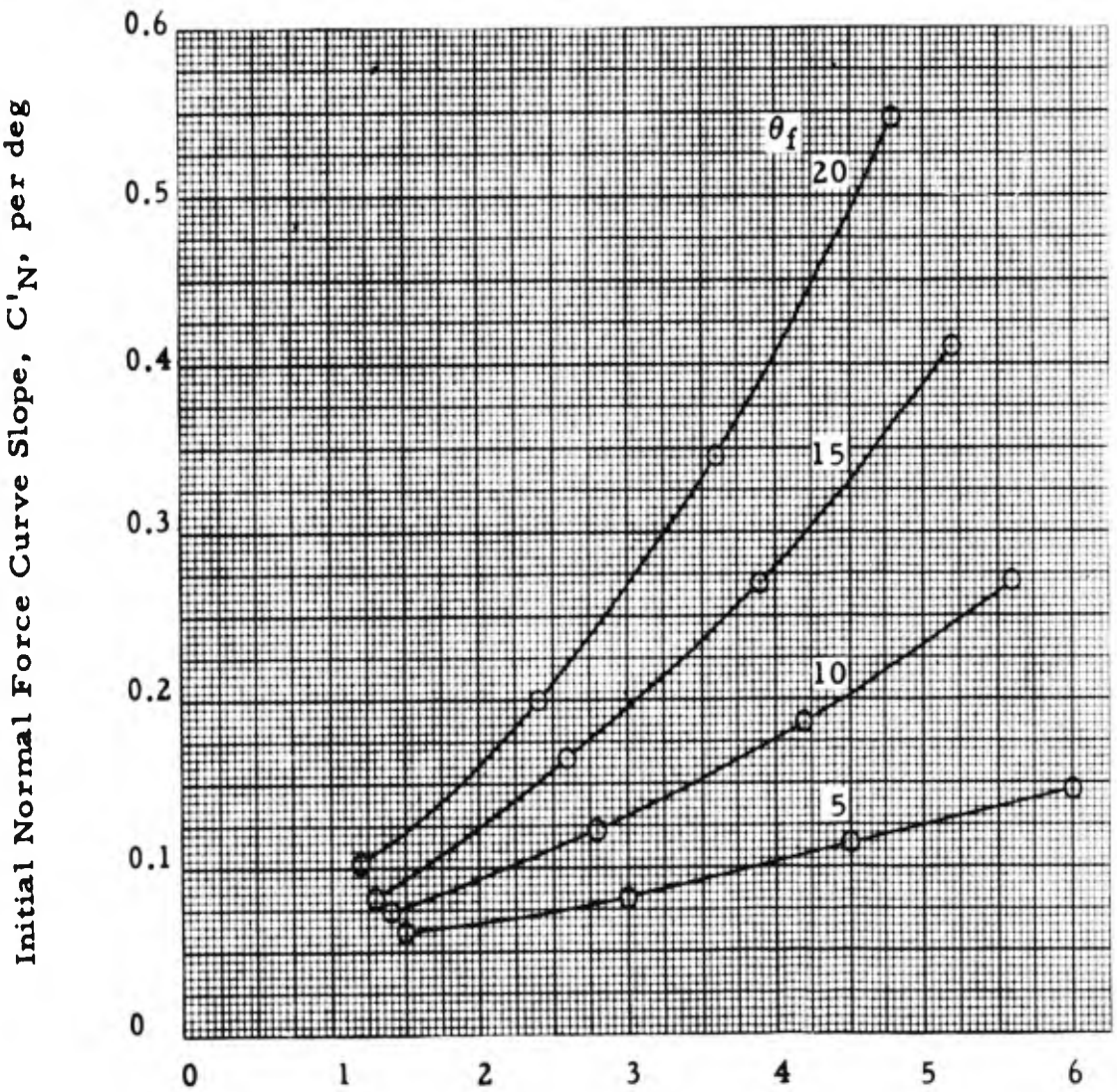

Fig. 16

Initial Center of Pressure for Models 21XX

$\theta_c = 22.5$, $L_{cy} = 1$

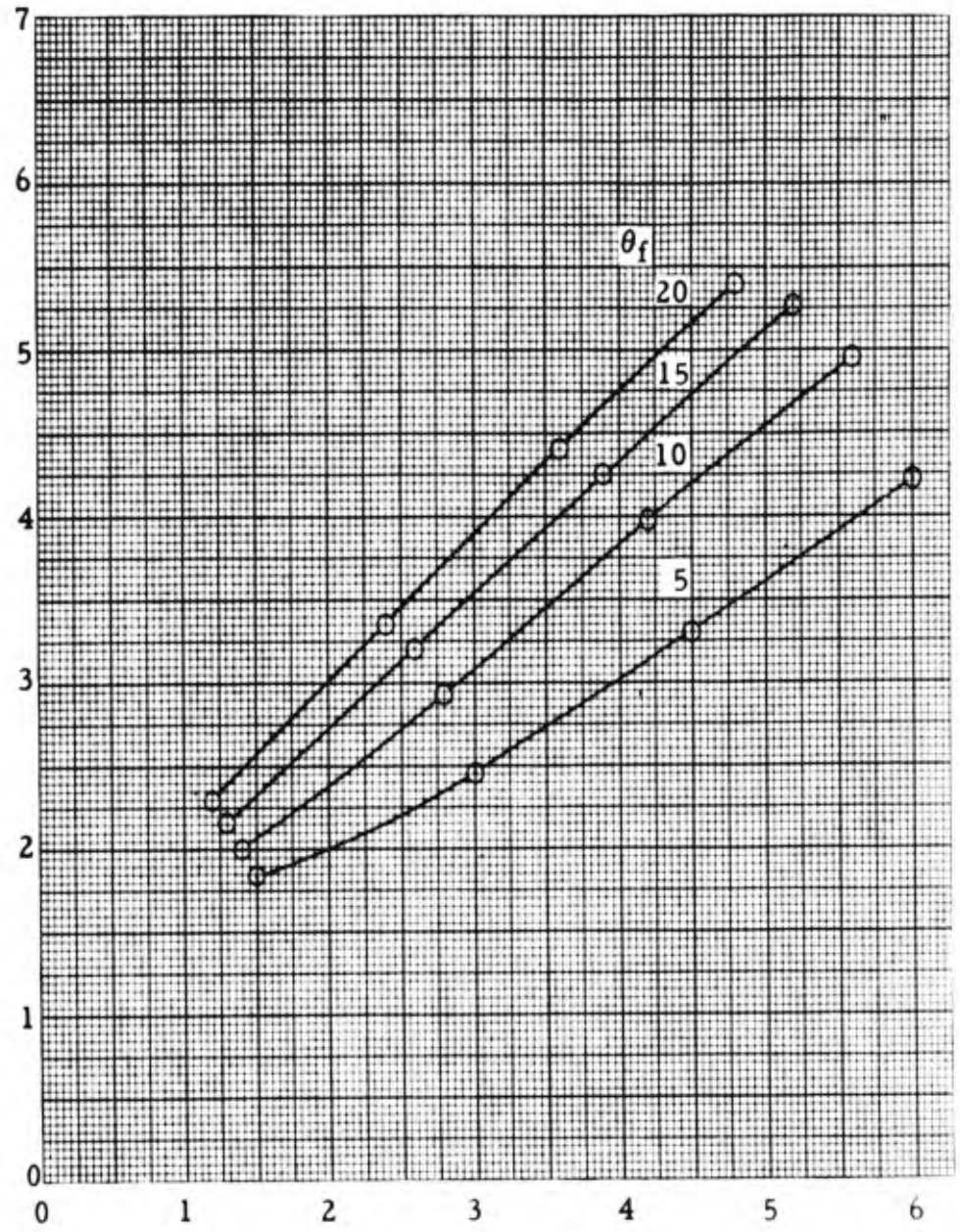

Fig. 17

Initial Center of Pressure for Models 22XX

$\theta_c = 22.5$, $L_{cy} = 2$

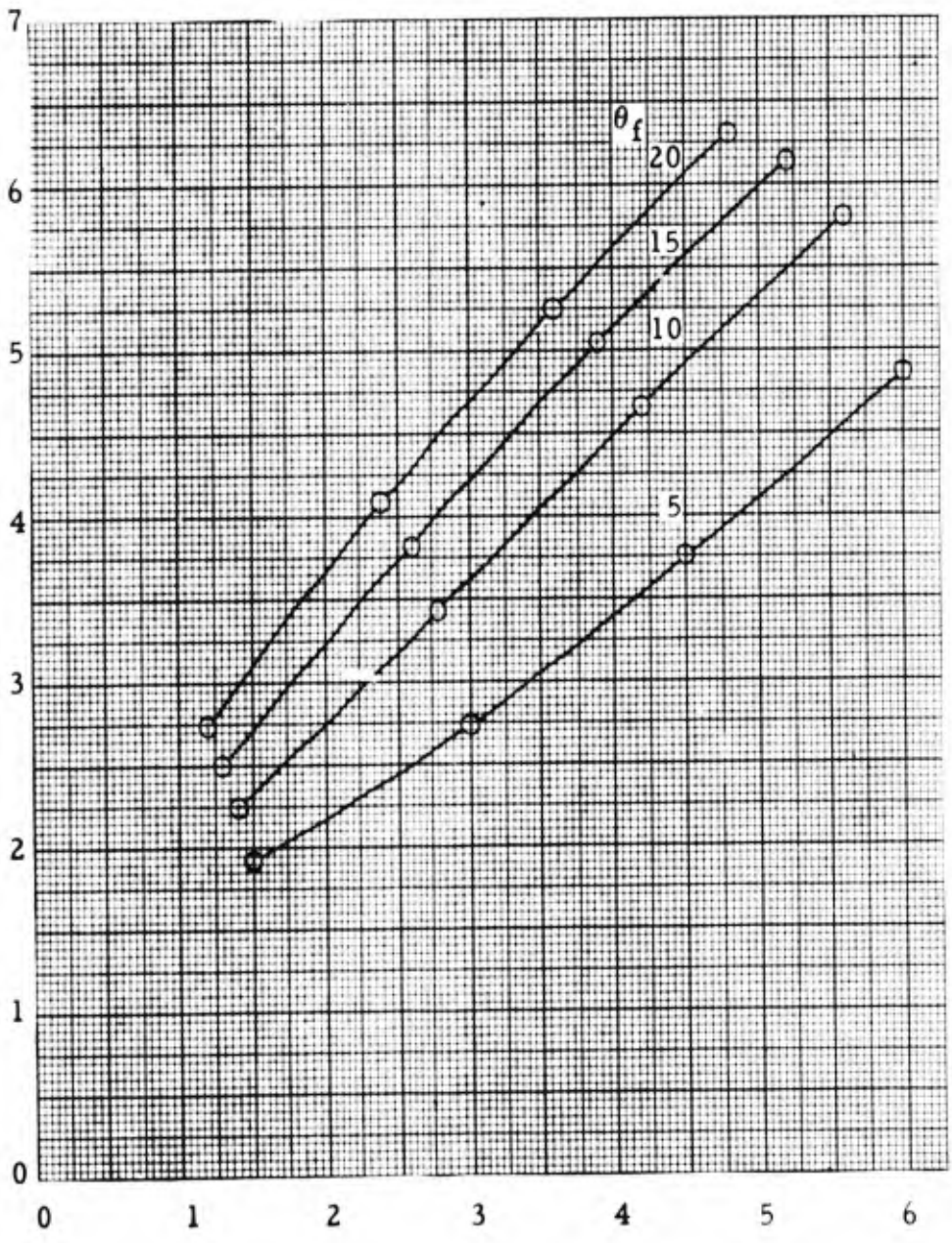

Fig. 18

Initial Center of Pressure for Models 23XX

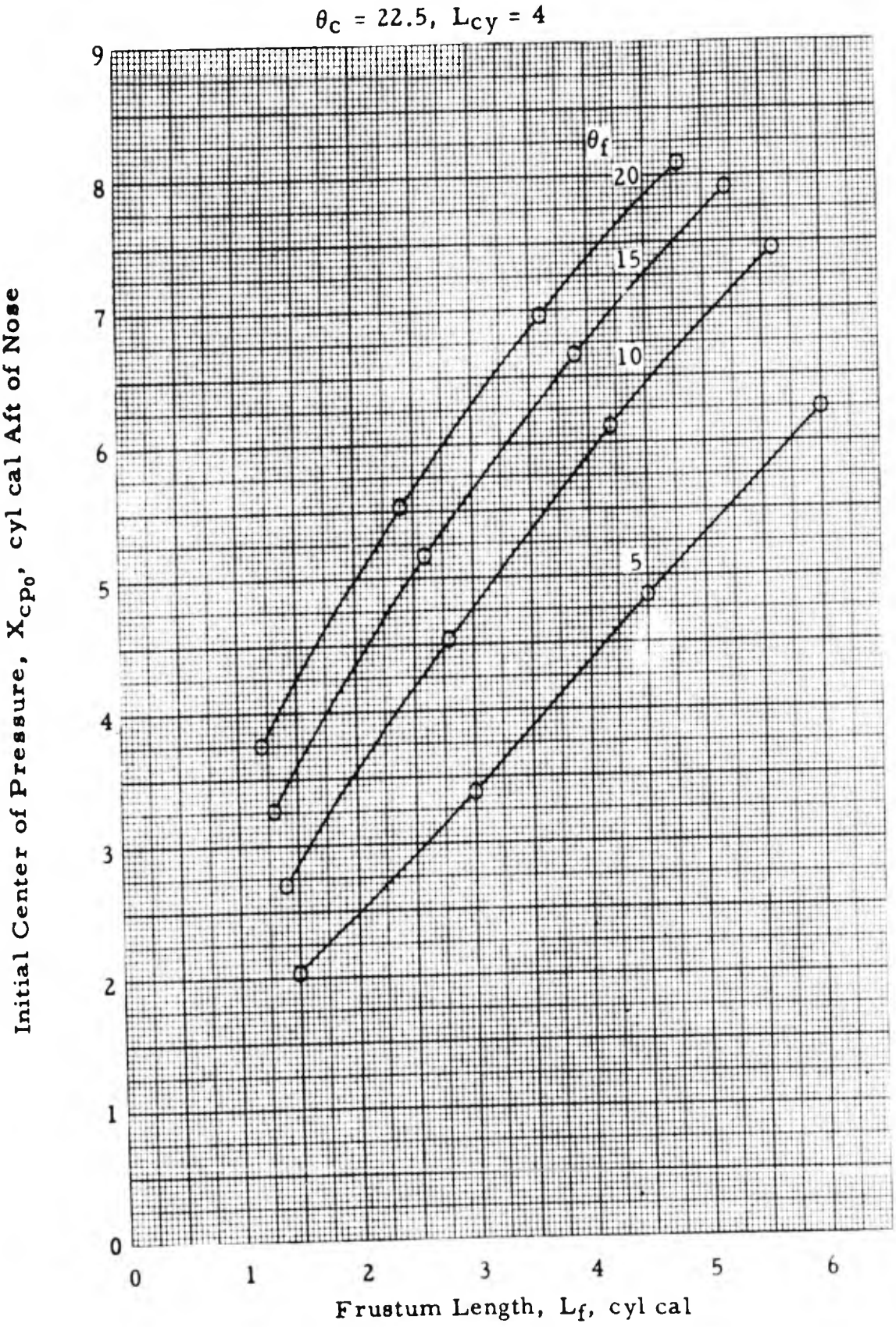

Fig. 19

Nonlinear Characteristics of Normal Force, Pitching Moment, and Center of Pressure

$\theta_c = 22.5$, $L_{cy} = 1$

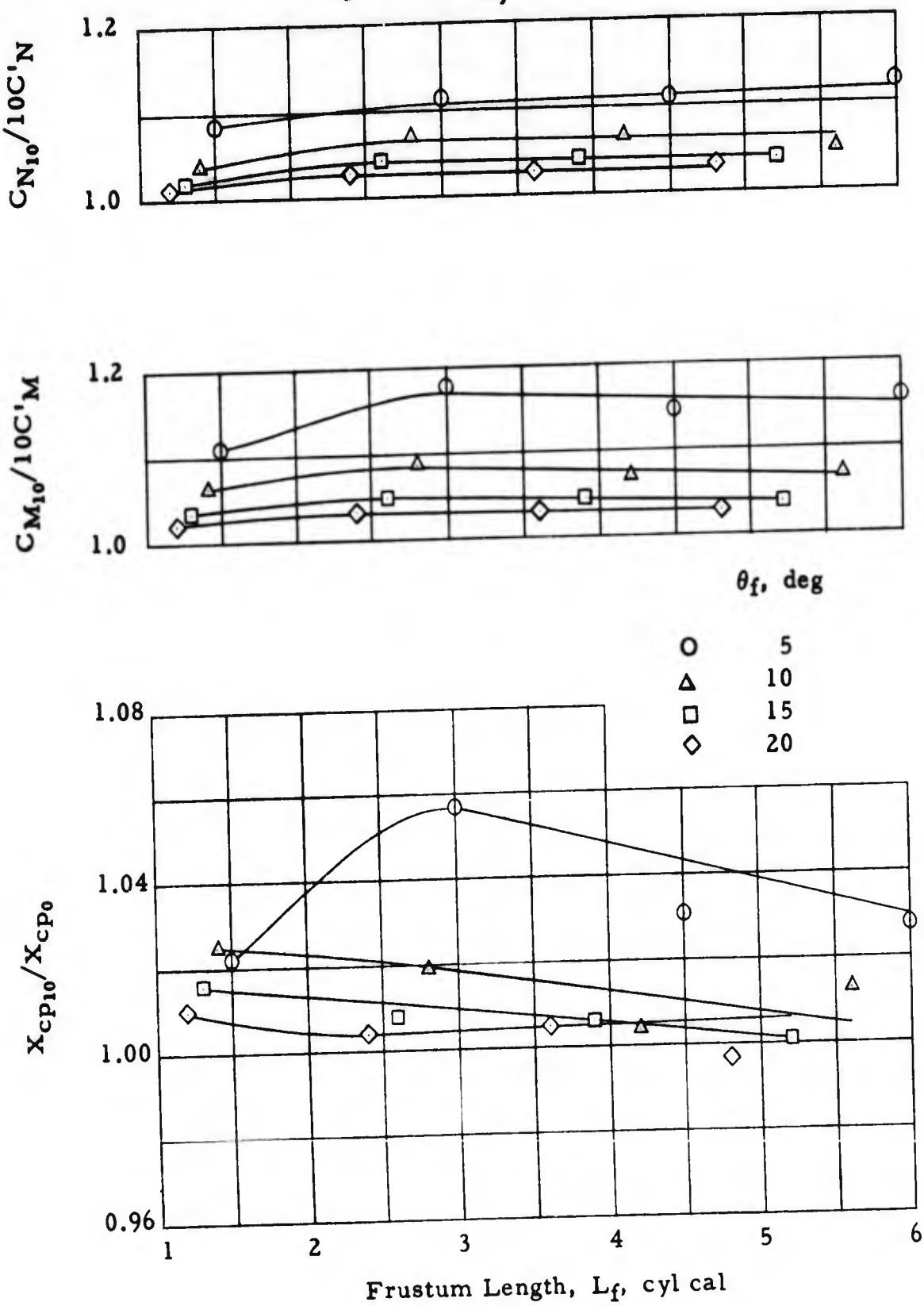

Fig. 20

Nonlinear Characteristics of Normal Force,
Pitching Moment, and Center of Pressure

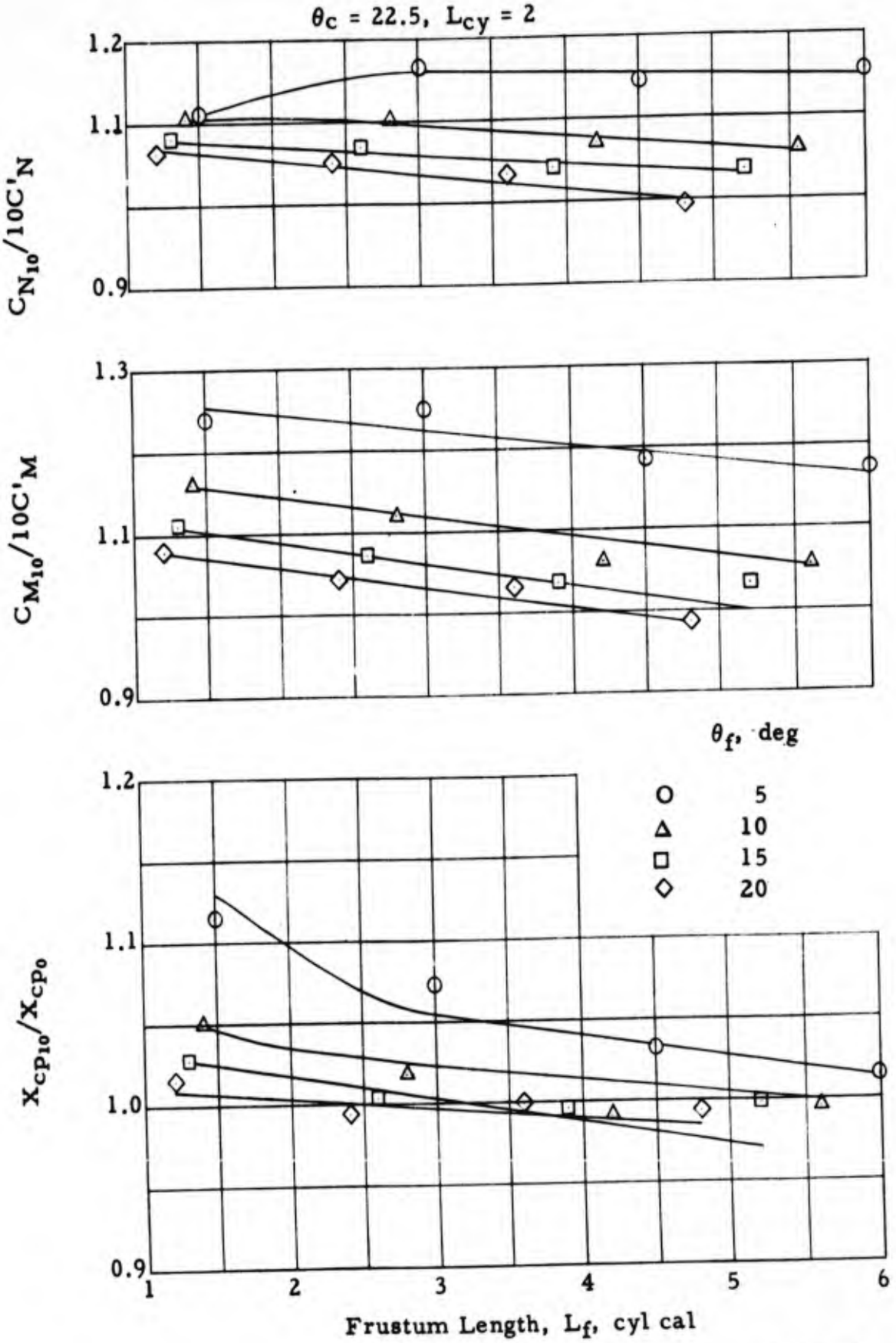

Fig. 21

Nonlinear Characteristics of Normal Force, Pitching Moment, and Center of Pressure

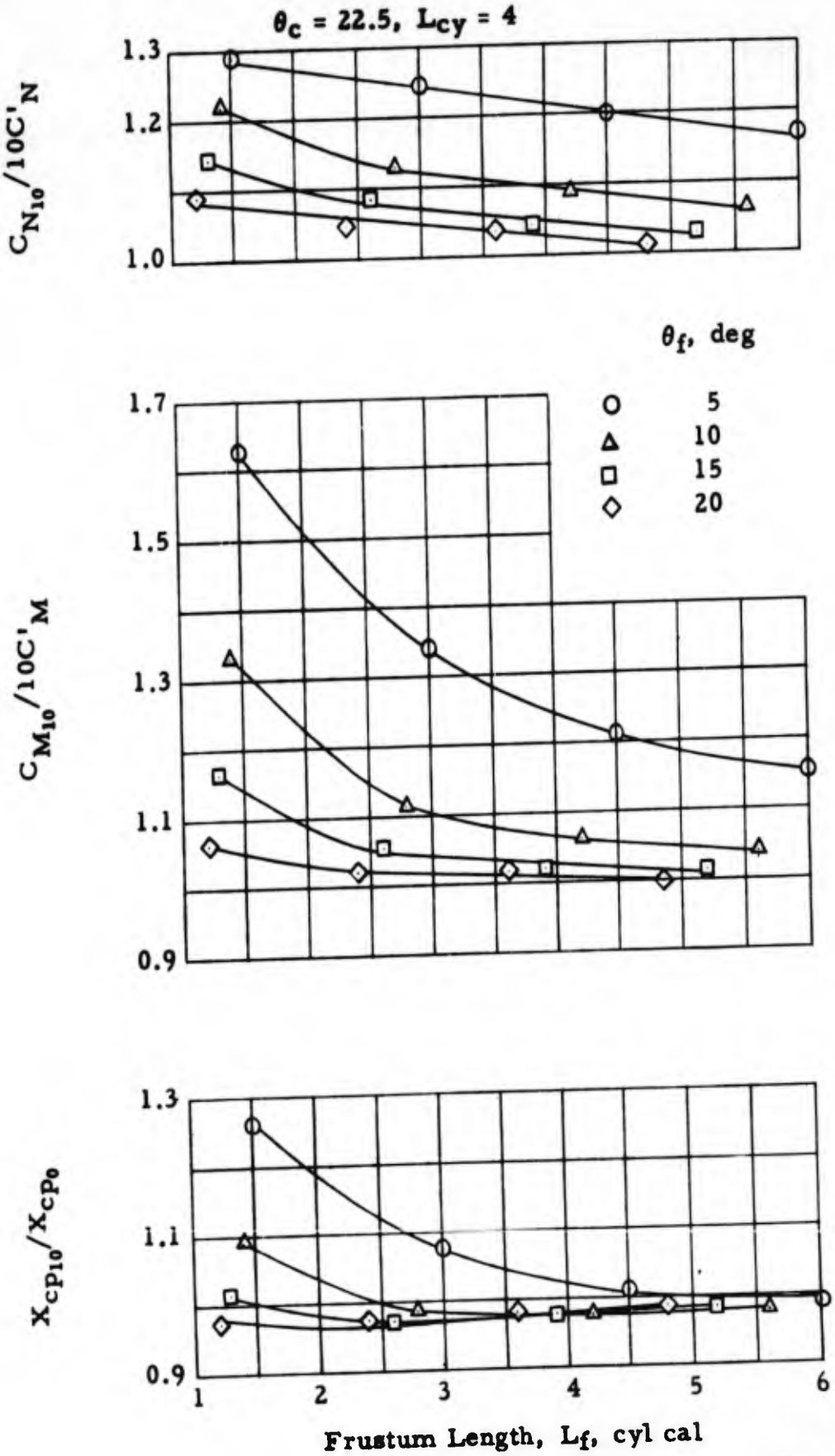

Fig. 22

ARMY-REDSTONE ARSENAL HUNTSVILLE, ALA.

DISTRIBUTION

	Copy
Guided Missile Technical Information Distribution List, MML 200/8, List No. 8, 1 September 1955, Parts A, C, and DA	1 - 137
Western Development Division Headquarters ARDC Post Office Box 262 Inglewood 45, California ATTN: Ramo-Wooldridge	138
Guided Missile Development Division	139
ATTN: E. G. Geissler	140
E. L. Linsley	
Research Laboratories ATTN: J. L. Potter	141
Rocket Development Laboratories ATTN: F. F. Fleming	142
Technical Feasibility Studies Office	143
ATTN: E. Stuhlinger	144
K. E. Patt	145
R. E. Lavender	146
J. L. Sims	147
R. A. Deep	148
J. H. Henderson	

AD 85739